Copyright
by
John Caleb Barentine
2008

A Comparative Astrochemical Study of the High Mass Protostellar Objects NGC 7538 IRS 1 and IRS 9

by

John Caleb Barentine, B.S.; M.S.

THESIS

Presented to the Faculty of the Graduate School of

The University of Texas at Austin

in Partial Fulfillment

of the Requirements

for the Degree of

MASTER OF ARTS

THE UNIVERSITY OF TEXAS AT AUSTIN

August 2008

A Comparative Astrochemical Study of the High Mass Protostellar Objects NGC 7538 IRS 1 and IRS 9

APPROVED BY

SUPERVISING COMMITTEE:

John H. Lacy, Supervisor

Neal J. Evans II

Acknowledgments

The efforts of a number of people who contributed to this work in one way or another are worthy of being acknowledged. First I wish to express my sincere thanks to my research adviser, John Lacy, for the steady hand of guidance he showed during the production of this thesis. He opened up the world of molecular spectroscopy to me and encouraged learning about a field of astronomy that was brand new to me. To Marty Bitner I owe a special acknowledgment as a mentor whose efforts helped make my transition back into graduate school much easier. His time and effort were also especially helpful in learning TEXES operations and data reduction. The observing runs during which our data were obtained benefitted tremendously from the experience and judgment of people such as Tommy Greathouse, Matt Richter and Shay Strong. With their help I came up to speed relatively quickly in handling TEXES and was made to feel welcome as part of a team. In addition to Dr. Lacy, I am grateful to Neal Evans, Dan Jaffe and Chris Sneden for their service on my research committee.

The success of observational astronomy depends strongly on the availability and cooperation of competent operations support staff. I would like to recognize the efforts of the highly professional staff at both the IRTF and Gemini who helped make our observing runs more efficient, and the people

of Mauna Kea Observatories Support Services for making our stays at Hale Pohaku more pleasant. I would also like to recognize the special and sacred significance of the summit of Mauna Kea within the indigenous Hawai‘ian community. We are truly fortunate to be permitted to carry out our observations from such a remarkable location.

Even though as graduate students we work as individuals on our research projects, I feel very fortunate to find myself among the fine group of people who make up my graduate class: Amanda Bayless, Guille Blanc, Sean Couch, Bi-Qing For, Candace Gray, Amanda Heiderman, Jeremy Murphy, Sehyun Hwang, Hyo-Jeong Kim, Masatoshi Shoji, Tim Weinzirl and Randi Worhatch. I learned something from them nearly every day during the preparation of this thesis and continue to do so. Stephanie Crouch and Charmarie Burke helped us navigate the bureaucracy of our first two years, much to our benefit.

My family and friends have been a source of tremendous encouragement during a difficult time, particularly my parents, John and Delsia Barentine, to whom I owe so much, and my grandparents, Gerald and Verne Anne Danley, early and frequent supporters of my astronomical journey. My brother, Brent, spent a year and a half along on the Austin adventure and I thank him for taking the plunge with me. And I thank in particular Reyne Telles for helping keep my head above water just when I needed it.

Finally I would like to offer my gratitude for the efforts and counsel of Dr. James Gay for his help keeping me on track during the preparations for

the public defense of this work and the writing of the thesis.

A Comparative Astrochemical Study of the High Mass Protostellar Objects NGC 7538 IRS 1 and IRS 9

John Caleb Barentine, M.A.
The University of Texas at Austin, 2008

Supervisor: John H. Lacy

The formation circumstances of high mass ($M \geq 8M_{\odot}$) stars are little understood in comparison to the more well-studied formation processes of low mass stars like the Sun. How the chemical composition of the enshrouding envelope influences the final characteristics of a high mass star after it settles onto the Main Sequence, how the chemistry of the envelope proceeds with time, and which materials survive the birth process and find their way into the circumstellar disk is not well-informed by observations at present. Here we report the results of a spectroscopic study of the high mass protostellar object NGC 7538 IRS 9 and compare our observations to existing data on the nearby object NGC 7538 IRS 1. The two objects originate within the same molecular cloud and are thought to be roughly coeval, offering an unusual opportunity to study the temporal evolution of envelope chemistry in objects presumably sharing an identical starting composition. The observations were

made with the Texas Echelon Cross Echelle Spectrograph (TEXES), a sensitive mid-infrared grating spectrometer capable of very high spectral resolution ($R = \lambda/\Delta\lambda \simeq$ 100,0000, or Δv ~3-4 km s^{-1}). Forty-six individual lines in fundamental modes of the molecules C_2H_2, CH_4, HCN, NH_3 and ^{12}CO were detected, including isotopologues (^{13}CO, $^{12}C^{18}O$) and one combination band ($\nu_4+\nu_5$ C_2H_2). Fitting synthetic spectra to the data yielded the Doppler shift, excitation temperature, Doppler b parameter, column density and covering factor for each molecule observed; we also computed column density upper limits for lines and species not detected, such as HNCO and OCS. The results were compared against a similar study of IRS 1. We find differences among spectra of the two objects likely attributable to their differing radiation and thermal environments. Temperatures and column densities for the two objects are generally consistent, while the larger line widths toward IRS 9 indicate less saturated lines than those toward IRS 1. Finally, we propose a radiative transfer mechanism to explain the particular pattern of absorption and emission seen in mid-infrared transitions of the ν_2 "umbrella" mode of ammonia (NH_3) toward IRS 9.

Table of Contents

Acknowledgments **iv**

Abstract **vi**

List of Tables **x**

List of Figures **xi**

Chapter 1. Introduction **1**

1.1 The Importance of Chemistry in Understanding Massive Star Formation 3

1.2 Properties of NGC 7538 IRS 9 5

1.3 Comparison of IRS 9 and IRS 1 9

Chapter 2. Observations and Reductions **11**

2.1 Data Reduction 15

2.2 Spatial Resolution of IRS 9 16

Chapter 3. Description of the Data **20**

3.1 C_2H_2 22

3.2 HCN 24

3.3 CH_4 25

3.4 NH_3 26

3.5 CO 27

3.6 OCS 32

3.7 HNCO 35

Chapter 4. Analysis **36**
4.1 Spectral Line Fitting 37
4.1.1 Simple Synthetic Spectrum Fitting 37
4.1.2 χ^2 Minimization Spectral Fitting 39
4.1.3 Column Density Upper Limits For Non-Detections . . . 51
4.1.4 An Upper Limit to the Ionizing Flux in IRS 9 56
4.2 Interpretation of the Spectroscopic Results 59
4.3 A Radiative Pumping Scheme for NH_3 63

Chapter 5. Summary **68**

Vita **77**

List of Tables

2.1 Circumstances of TEXES observations of NGC 7538 IRS 9 . . 12

2.2 Circumstances of TEXES observations of NGC 7538 IRS 1. All observations of IRS 1 were made with TEXES at the IRTF except the three dates in 2007 which were obtained at Gemini. 13

4.1 Molecular absorption parameters derived from simple synthetic spectrum fitting in LTE 40

4.2 Molecular absorption parameters determined from χ^2 minimization spectral fitting. Quantities in parentheses are the 1σ uncertainties on the adjacent figures in the same units. 52

4.3 3σ upper limits to line equivalent width and column density of molecules in the upper state for selected non-detections. A uniform temperature of 200 K was assumed for all species. . . 54

4.4 Abundances in IRS 9 and IRS 1 with respect to CO and H_2 . 61

4.5 Predicted fluxes for the P, Q, R lines of ν_2 transitions of NH_3 ($J_u = 3$) and measured fluxes for the corresponding P-branch lines from TEXES spectra. Positive flux values indicate net emission while negative values indicate net absorption in a given line. . 67

List of Figures

1.1 The ISO-SWS spectrum of NGC 7538 IRS 9 between 2.4 and 45 μm. The identifications of some features are marked. 8

2.1 Contour plot of the TEXES scan map of NGC 7538 IRS 9 at 745.8 cm^{-1} after maximum entropy deconvolution. The PSF reference for the deconvolution was a scan map of the mid-infrared standard μ Cephei made with the same parameters as the IRS 9 scan. North is up and east at left and contours are plotted at flux densities of 25, 50, 100, 150, 200, 250 and 300 Jy. The plot origin is approximately the location of the source peak intensity. 19

3.1 The normalized TEXES spectrum centered approximately at 744.8 cm^{-1} toward NGC 7538 IRS 9 obtained on UT 2007 October 21 at Gemini North is shown in the upper trace. The asterisks mark positions of the following features, left to right: C_2H_2 ν_5 $R(5)$, HCN ν_2 $R(10)$, and C_2H_2 ν_5 $R(6)$. Atmospheric transmission is represented by the lower trace on the same scale. The wavenumber scale has been corrected for the Earth's motion with respect to the LSR. 21

3.2 Spectrum of the ν_5 Q branch of C_2H_2 observed with TEXES toward NGC 7538 IRS 9 (thin lines). A fit is superimposed from an LTE model with $T = 100$ K, $b = 1$ km s^{-1}, and $N(C_2H_2) = 2 \times 10^{15}$ cm $^{-2}$ (thick lines). The synthetic spectrum has been convolved with the TEXES instrumental lineshape function. . 22

3.3 Spectra of three features in the ν_4 band of CH_4 toward IRS 9, shown on an LSR velocity scale as labeled. For the spectrum containing the $R(2)$ lines, the velocity scale has been set to the LSR value for the stronger component (rest frequency 1322.085 cm^{-1}). 26

3.4 TEXES data toward NGC 7538 IRS 9 at the position of the $^{14}NH_3$ ν_2 antisymmetric Q branch (top panel) and symmetric $P(7,K)$ branch (bottom panel). The upper curve in each plot shows the data, while the lower curve in each shows the relative atmospheric transmission on the same scale. Asterisks mark positions of the NH_3 lines. Both spectra have been corrected for the Earth's motion relative to the LSR, and the position of the NH_3 lines shifted to the systemic LSR velocity of approximately -60 km s^{-1}. 28

3.5 The upper panel shows spectra of two P-branch lines of ^{12}CO and one P-branch line of ^{13}CO toward IRS 9 obtained with TEXES. The lower panel shows the same spectral settings observed toward IRS 1. In both cases the motion of the Earth with respect to the LSR has been removed from the velocity scales. 31

3.6 TEXES spectrum toward NGC 7538 IRS 9 centered near the 5 μm rotational lines of several isotopologues of CO. The data are shown in the upper trace (solid line) and the relative atmospheric transmission in the lower trace (dot-dashed line), multiplied by a factor of 10. Some line identifications are shown. . 32

3.7 The TEXES spectra of NGC 7538 IRS 1(top) and IRS 9 (bottom) near features in the P-branches of ^{12}CO and ^{13}CO. The wavenumber scale has been corrected to a velocity reference at rest in each object's frame. Line centers of OCS features in this spectral window are marked with asterisks. The periodic regions of strong noise are due to absorption by telluric atmospheric CO_2. 34

4.1 TEXES spectra of NGC 7538 IRS 9 (thin lines) and synthetic spectra obtained by the simple LTE fitting method described in Section 4.1.1 (thick lines). The continuum in each spectrum has been normalized to unity and the spectra are plotted on a velocity scale referred to the LSR. Features shown are C_2H_2 ν_5 $R(1)$, $R(5)$, $R(6)$ and $R(13)$. 41

4.2 TEXES spectra of NGC 7538 IRS 9 (continued). Features shown are C_2H_2 $\nu_4 + \nu_5$ $P(2)$ and $P(3)$, HCN ν_2 $R(16)$ and CH_4 ν_4 $R(0)$. 42

4.3 TEXES spectra of NGC 7538 IRS 9 (continued). Features shown are the two components of CH_4 ν_4 $R(2)$, NH_3 ν_2 a$P(4,0)$ and a$P(4,1)$. 43

4.4 TEXES spectra of NGC 7538 IRS 9 (continued). Features shown are NH_3 ν_2 a$P(4,3)$, s$P(7,0)$, s$P(7,1)$ and s$P(7,2)$. . . . 44

4.5 TEXES spectra of NGC 7538 IRS 9 (continued). Features shown are NH_3 ν_2 s$P(7,3)$, s$P(7,4)$, s$P(7,5)$ and s$P(7,6)$. . . . 45
4.6 TEXES spectra of NGC 7538 IRS 9 (continued). Features shown are $^{12}C^{16}O$ v=1-0 $P(14)$, $P(15)$, $P(21)$ and $P(22)$. . . . 46
4.7 TEXES spectra of NGC 7538 IRS 9 (continued). Features shown are $^{13}C^{16}O$ v=1-0 $P(3)$, $P(4)$, $P(11)$, $P(12)$. 47
4.8 TEXES spectra of NGC 7538 IRS 9 (continued). Features shown are $^{12}C^{18}O$ v=1-0 $P(2)$ and $P(3)$. 48

Chapter 1

Introduction

Stars are the ultimate origin of all elements heavier than lithium; without them there would likely be no life in the universe. Their life cycles result in stars as self-propagating entities in which each successive generation is recycled from the remains of the previous. Details of the life cycles of low-mass stars such as the Sun (M=1$M_{\odot}$) have been gleaned from decades of research, thanks in part to the relative amenability of low mass protostellar objects to study. However, the formation of high mass stars is not as well understood at present, in part because high mass stars are not generally forming near the solar neighborhood. Challenged by the limitations of telescopes and instrumentation, progress in understanding this subject was also slowed by the required sophistication of theory and limited computational power. Rapid change in all these areas over the past two decades is quickly changing our understanding of the origins of massive stars.

Along with the atomic processes at work in the formation of stars, a rich panoply of molecules formed in the protostellar environment participates in complex chemical reaction networks; those that survive the stellar birth process may be incorporated into circumstellar disks and, possibly, nascent

protoplanets. Some of these molecules have been implicated in the origin of life on the Earth, bringing into focus one of the central questions in modern science: did life arise elsewhere in the cosmos, and if so, under what circumstances? The answer to this question at least in part is one of chemistry: without knowledge of chemistry in starforming regions, no understanding of prebiotic chemistry can be complete.

In this work we sought to compare the chemical evolutionary states of the envelopes of high mass protostellar objects (HMPOs) forming in the same molecular cloud such that the starting abundances were presumed similar. Two such objects that fit this description are NGC 7538 IRS 1 and IRS 9. These young objects are believed to be in similar stages of their evolutionary histories, though IRS 9 is either of lower mass than IRS 1 or in an earlier stage. We performed mid-infrared molecular absorption line spectroscopy of these objects and from our spectra derived molecular abundances for comparison with chemical models and excitation parameters to characterize the media in which the observed spectral lines arise. In this way we examined how the evolutionary state of a HMPO envelope determines the observed chemistry of the gas.

In Chapter 1 we briefly discuss the current understanding of high mass star formation with particular emphasis on the role played by chemistry, followed by an introduction to the objects we observed. In Chapter 2 we describe the observations and data reduction, while descriptions of the molecular features seen in our spectra are given in Chapter 3. The data analysis and in-

terpretation are discussed in Chapter 4 including derivation of the excitation parameters for the molecules we observed. We summarize in Chapter 5.

1.1 The Importance of Chemistry in Understanding Massive Star Formation

Stars are responsible for the atomic constitution of the universe for all elements other than those presumed to have formed in the Big Bang: hydrogen, helium and primordial lithium. The formation of high-mass stars ($M > 8M_{\odot}$) populates galaxies with the sites of heavy element nucleosynthesis and key starting materials for both organic and inorganic chemical reactions via the triple-α (carbon) and CNO cycles (oxygen and nitrogen) (Zinnecker & Yorke 2007). Silicon and carbon made in the interiors of massive stars constitute most dust grains in the universe (Draine 2003), their surfaces the sites of some chemical reactions in molecular clouds and "freeze out" of molecules from the gas phase. Furthermore, shocks and flows in supernova events precipitated by massive star death distribute these atomic species into the disk of the Galaxy (Arnett 1996), catalyze chemical reactions in the interstellar medium, and provide a potential source of turbulence to encourage future star formation (Scalo & Elmegreen 2004). Recent evidence suggests that like their low-mass kin, young massive stars are often accompanied by circumstellar disks (Jiang et al. 2008), supporting the idea that planets and smaller bodies may form around these stars. Meanwhile, the same material that comprises the disk feeds accretion onto the nascent star at the center of the envelope in its final

phases as the star approaches the Main Sequence (MS) in the Hertzsprung-Russell diagram and ignites hydrogen burning, then continues to accrete to its final mass, moving parallel to the MS (Zinnecker & Yorke 2007).

The composition of the envelope and disk, then, are of considerable interest in understanding these processes. Regions of recent, massive star formation comprise a diverse and complex chemistry (van Dishoeck & Blake 1998). Molecules are made in the gas phase in dark molecular cloud cores as well as on grain surfaces; gas phase molecules freeze out on the grains and are held fast until the onset of star formation. Rising temperatures then liberate different molecular species at different radii from rapidly developing protostellar objects, leading to a radially dependent chemical composition. The highest temperatures are found closest to the embedded protostar; in these regions a unique "hot core" chemistry takes place (Charnley 1995). These are small ($r < 0.1$ pc), dense ($n_{H_2} > 10^7$ cm^{-3}) and relatively hot ($T > 100$ K) zones strongly affected by the radiation environment of the embedded protostellar object (Kurtz et al. 2000). Certain molecular species are only expected in quantity once this phase sets in, as temperatures in colder regions of the envelope are too low for the required reactions to proceed efficiently (Schöier et al. 2002). The presence of outflows and circumstellar disks further complicates the chemical picture by providing the physical conditions for both the synthesis and destruction of additional species. Eventually the protostar becomes a significant source of ionizing radiation and stellar winds, potentially destroying some molecules but offering the possibility of recombination elsewhere in the

form of more complex species.

Our insight into chemical reaction networks and synthesis pathways has been limited by observational challenges, particularly in the innermost regions where hot core chemistry is believed to take place. Millimeter studies of starforming regions offer the sensitivity to weak lines and the ability to produce maps in molecular line transitions, but beam sizes are often too large to permit useful single sightline observations. The low-lying, pure rotational transitions of molecules observed in this wavelength regime are particularly useful for probing deeply embedded protostellar objects. Rovibrational lines of various molecular species in the mid-infrared are detected along pencil-beam sightlines toward embedded continuum sources, allowing us to observe the innermost regions around protostellar objects. Gas-phase molecular lines, however, often tend to cluster together densely, making a case for high spectral resolution to adequately resolve individual lines. Such observations would deliver velocity resolution of order a few km s^{-1} to detect specific lines as well as provide useful kinematic information from lineshapes. On the other hand, achieving high spectral resolution comes at the cost of lost sensitivity, limiting observations to the few nearby molecular cloud complexes currently undergoing massive star formation. Making statistical inferences from a limited sample carries its own risks, so high resolution observations should be well planned and molecular species carefully selected for observations to be useful and efficient.

1.2 Properties of NGC 7538 IRS 9

The bright H II region NGC 7538 is associated with a larger starforming complex that appears to harbor an embedded young star cluster of several hundred members (Balog et al. 2004). We will refer to the entire complex as NGC 7538. Several infrared sources (IRS) have been identified within the complex in which it is believed the formation of high mass stars is taking place. Ojha et al. (2004) derive an age of $\sim$1 Myr for this embedded stellar population. A survey of literature values for the distance to NGC 7538 in the last decade gives a weighted mean of 3.0$\pm$0.3 kpc (Heyer et al. 2001, Brunt 2003, Foster & Routledge 2003, Balog et al. 2004, Reid & Wilson 2005, Kameya 2006, Araya et al. 2007). Individual infrared sources NGC 7538 are relatively bright given their distance from Earth, making them available for high resolution spectroscopic study.

IRS 9 is a molecular cloud core embedded in NGC 7538 where one or more massive stars is currently forming. The velocity of IRS 9 with respect to the Local Standard of Rest (LSR) is about -57 km s^{-1} (van der Tak et al. 2000), so spectral lines observed toward this source with telluric atmospheric counterparts (e.g., CO and CH_4) are usually well separated from those lines. Weak free-free emission is observed ($\sim$2 Jy at 22.2 GHz; Kameya et al. 1990), suggesting that a compact H II region has not formed around the embedded central object or objects. Its total luminosity is about 4×10^4 $L_\odot$ (Sandell et al. 2005), and it is a bright IRAS 12 μm source at $\sim$60 Jy (Beichman et al. 1988). A zero-age Main Sequence (ZAMS) star with this luminosity (i.e.,

deriving its luminosity from hydrogen burning) would have a spectral type of B0.5 and an effective temperature T_{eff} = 26200 K (Panagia 1973). Boogert et al. (2004) suggest the existence of an inner, warm molecular emission region with a radius of ∼70 AU; the dust temperature at this distance for an object of IRS 9's luminosity would be ∼1000 K depending on the dust mass opacity.

Millimeter-wavelength data show that IRS 9 is a site of active, massive star formation (Sandell et al. 2005) in which young stellar objects (YSOs) are driving a set of bipolar molecular outflows on a dynamical timescale of ≤ 20,000 years. At least one of these outflows appears to be highly energetic. Mitchell & Hasegawa (1991) report the discovery of an outflow in IRS 9 with a velocity of 110 km s^{-1}, which they interpret to have emerged as recently as 1,200 years ago, perhaps indicating the beginning of a recent episode of accretion. The multiple outflows imply that IRS9 may in fact be a cluster of young objects.

Early efforts such as those of Willner (1976) were the first to reveal the infrared spectra of objects like IRS 9. Our view was greatly enhanced by the deployment of the first space-based mid-infrared spectroscopic observatory, the *Infrared Space Observatory* (ISO), in the mid-1990's. While ISO achieved only modest spectral resolution, it offered a new window on the composition of massive YSOs. Figure 1.1 shows the infrared spectrum of IRS 9 obtained with the Short Wavelength Spectrometer (SWS) onboard ISO (Whittet et al. 1996). A number of both solid-phase and gas-phase molecules are seen; the variety and number of constituents indicate a diverse chemistry even in the early stages

of massive star formation. Gibb et al. (2004) list sixteen molecules seen in the solid phase alone. Tielens (2005) compares the observed ice compositions of

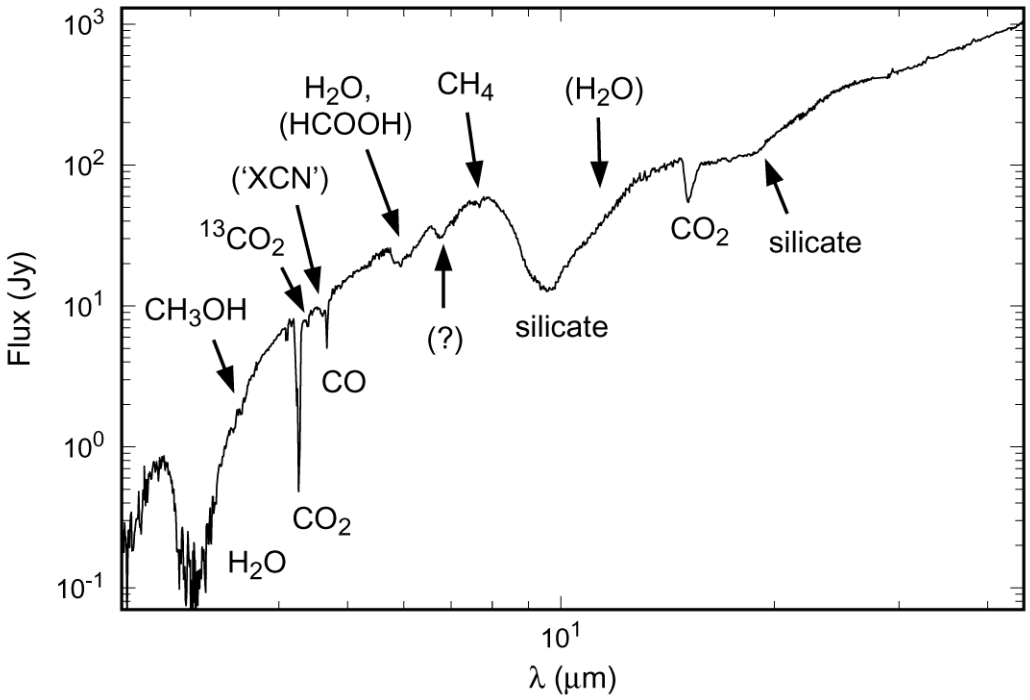

Figure 1.1 The ISO-SWS spectrum of NGC 7538 IRS 9 between 2.4 and 45 μm. The identifications of some features are marked.

IRS 9, the massive protostar W33 A and comet C/1995 O1 Hale-Bopp, finding generally good agreement both in the molecular species represented and their relative abundances. This result lends support to the idea that comets are rather pristine, chemically unaltered bodies whose composition more closely reflects interstellar cloud composition than that of other Solar System objects.

Boogert et al. (2004) used the NIRSPEC instrument on the Keck 10 m telescope at R=25000 to follow up the ISO observations of IRS 9 in the 3.2

μm CH_4 ν_3 C-H stretch feature. They resolved gas-phase lines and found a pattern in which low J lines were seen in absorption whereas at higher J the lines went into emission. They argue for formation of CH_4 by hydrogenation of atomic C on grain surfaces and note its absence in the high velocity outflow, explaining that it "burns" in shocked conditions to become CO. Other molecular species seem to be observed in the act of desorption from grains into the gas phase. Spectral features attributable to NH_3 frozen in a polar, water-rich ice mixture were detailed by Lacy et al. (1998). Gas phase NH_3 is also observed toward IRS 9, indicating active sublimation of ices from grains is taking place; however, no reports of observations of inversion transitions of NH_3 at centimeter wavelengths are evident in the literature.

1.3 Comparison of IRS 9 and IRS 1

The evolutionary state of the nearby source NGC 7538 IRS 1 appears to contrast with that of IRS 9, allowing a direct comparison of the physical conditions and chemical constituents of two similar systems under similar initial conditions. IRS 1 has already been extensively studied in the mid-infrared by Knez et al. (2008) and appears to be a forming, late O star undergoing active accretion (Lacy & Jaffe 2007). There likely exists an accretion disk and/or envelope around the star on account of the strong molecular absorption observed toward the continuum source, evident partial covering of the source by the absorbing material, and previous observations and models indicating a disk (Pestalozzi et al. 2004, Lugo et al. 2004, De Buizer & Minier 2005). Its

higher luminosity of 8×10^4 $L_\odot$ corresponds to a spectral type of O7.5 for a Main Sequence object (Werner et al. 1979, Lugo et al. 2004). Campbell (1984) reports ionized molecular outflows, in contrast to IRS 9's neutral molecular outflow. A wide range of gas temperatures toward IRS 1 is found in the literature: 800 K (C_2H_2 Q-branch) and 600 K (HCN), Lahuis & van Dishoeck (2000); 500 K (C_2H_2), Boonman et al. (2003); and 25/176 K ($^{12}CO/^{13}CO$), Mitchell et al. (1990). The range of temperatures likely indicates that some molecules are found in the warmer inner regions near the heating source while others, such as CO, are found in colder areas at large radii in the envelope.

The strong absorption due to ice in IRS 9 (Whittet et al. 1996) is comparatively weak in IRS 1, suggesting that a significant event occurs between these points on the evolutionary journey of high-mass stars. The reaction direction that previously favored molecules formed in the gas phase in the molecular cloud sticking to grain surfaces is reversed, flooding the environment with new constituents for further gas-phase reactions. We set out to observe systems on either side of this dividing line to understand better this defining moment of high mass star formation. Yet starting abundances are a factor that must be controlled for a proper one-to-one comparison; IRS 1 and IRS 9, originating in the same cloud with essentially identical abundances, are ideal laboratories for this kind of study.

Chapter 2

Observations and Reductions

We observed NGC 7538 IRS 9 with the Texas Echelon Cross (X) Echelle Spectrograph (TEXES; Lacy et al. 2002) on the *Gemini North* 8 m telescope in 2007 October. Similar observations of IRS 1 were carried out at the NASA Infrared Telescope Facility (IRTF) 3 m telescope in 2001 June, 2001 November, 2002 September, 2002 December and 2005 November. Circumstances for all IRS 9 observations are given in Tables 2.1. Concurrent IRTF observations of IRS 1 on the 2001 dates formed the basis for the work of Knez et al. (2008); details of these observations are given in Table 2.2. Additional observations of IRS 1 were made at Gemini in 2007 October to supplement previous TEXES data obtained at the IRTF.

TEXES is a high-resolution cross-dispersed grating spectrograph designed to operate at high spectral resolution (R = 75,000-100,000) over a range of mid-infrared wavelengths from 5 to 25 μm, as described by Lacy et al. (2002). Light diffracts off a coarsely-ruled "echelon" grating (Michelson 1898) at a large incidence angle with respect to normal at order $n \sim 1500$. The light then diffracts off a cross dispersion grating and is imaged onto a 256×256 pixel Si:As detector as a series of orders. At a given spectral set-

Table 2.1. Circumstances of TEXES observations of NGC 7538 IRS 9

UT Date	Telescope	Wavenumber Center (cm^{-1})	Included Features
2001 June 15	IRTF	768	C_2H_2 ν_5 R(15,16)
		780	[Ne II] ($^2P_{1/2} \rightarrow {}^2P_{3/2}$), C_2H_2 ν_5 R(21,22), HCN ν_2 R(22,23)
2001 June 18	IRTF	744	C_2H_2 ν_5 R(5,6)
2001 June 26	IRTF	761	C_2H_2 ν_5 R(12,13), HCN ν_2 R(15,16), HD, $H^{13}CN$ ν_2 R(18)
2001 June 28-29	IRTF	734	C_2H_2 ν_5 R(1), HCN ν_2 R(6,7)
2007 October 21	Gemini	828	HNCO ν_4 P-branch, $^{14}NH_3$ ν_2 sP(7,K)
		1308	$^{12}CH_4$ ν_4 R(0), $^{13}CH_4$ ν_4 R(1)
2007 October 25	Gemini	930	$^{14}NH_3$ ν_2 aQ(J,K)
		743	C_2H_2 ν_5 R(5,6)
2007 October 26	Gemini	853	$^{14}NH_3$ ν_2 aP(4,K)
		1323	$^{12}CH_4$ ν_4 R(2), $^{13}CH_4$ ν_4 R(4), C_2H_2 $\nu_4 + \nu_5$ P(1-3)
2007 October 27	Gemini	2055	OCS ν_2 P(12-22), ^{12}CO v=1-0 P(21,22), ^{13}CO P(11,12), $C^{18}O$ P(10,11), $C^{17}O$ P(16)
2007 October 28	Gemini	730	C_2H_2 ν_5 Q-branch
2007 October 30	Gemini	2085	^{12}CO v=1-0 P(14-15), ^{13}CO P(3,4), $C^{18}O$ P(2,3), $C^{17}O$ P(8,9)

Table 2.2. Circumstances of TEXES observations of NGC 7538 IRS 1. All observations of IRS 1 were made with TEXES at the IRTF except the three dates in 2007 which were obtained at Gemini.

UT Date	Wavenumber Center (cm^{-1})	Included Features
2001 June 15	780	[Ne II] ($^2P_{1/2} \rightarrow {}^2P_{3/2}$), C_2H_2 ν_5 R(21,22), HCN ν_2 R(22,23)
	768	C_2H_2 ν_5 R(15,16)
2001 June 18	744	C_2H_2 ν_5 R(5,6)
2001 June 26	761	C_2H_2 ν_5 R(12-14), HCN ν_2 R(15,16), HD, $H^{13}CN$ ν_2 R(18)
2001 June 28	734	C_2H_2 ν_5 R(1), HCN ν_2 R(6,7), $H^{13}CN$ ν_2 R(9)
	860	H_2O, OH
2001 June 29	734	C_2H_2 ν_5 R(1), HCN ν_2 R(6)
2001 November 21	731	C_2H_2 ν_5 Q-branch
2002 September 8	780	[Ne II] ($^2P_{1/2} \rightarrow {}^2P_{3/2}$), C_2H_2 ν_5 R(21,22), HCN ν_2 R(22-23)
	750	CH_3 ν_2 R-branch, C_2H_2 ν_5 R(7,8)
2002 September 9	930	$^{14}NH_3$ ν_2 aQ(J,K)
2002 September 10	1246	H_2 S(4)
2002 September 11	867	$^{14}NH_3$ ν_2 aP(5,K)
	530	SO_2 ν_2
2002 September 13	2055	OCS ν_2 P(12-22), ^{12}CO v=1-0 P(21,22), ^{13}CO P(11,12), $C^{18}O$ P(10,11), $C^{17}O$ P(16)
2002 September 14	807	Humphreys α
	819	C_2H_6 ν_9
	1280	$^{12}CH_4$ ν_4 P(4)
2002 December 9	813	H_2 S(2)
2002 December 10	587	H_2 S(1)
2002 December 20	1247	H_2 S(4)
2005 December 12	1310	$^{12}CH_4$ ν_4 R(0,2); $^{13}CH_4$ ν_4 R(0)
2007 October 21	827	HNCO ν_4 P-branch; $^{14}NH_3$ ν_2 sP(7,K)
2007 October 27	2055	OCS ν_2 P(12-22), ^{12}CO v=1-0 P(21,22), ^{13}CO P(11,12), $C^{18}O$ P(10,11), $C^{17}O$ P(16)
2007 October 30	2085	^{12}CO v=1-0 P(14-15), ^{13}CO P(3,4), $C^{18}O$ P(2,3), $C^{17}O$ P(8,9)

ting between five and ten cross-dispersed orders are imaged onto the detector for a spectral coverage of about 0.5%. The continuity of orders is wavelength-dependent; below 11 μm order overlap is sufficient to yield continuous coverage over an entire spectral setting. At wavelengths longer than 11 μm there are gaps between adjacent orders.

At Gemini the pixel scale of TEXES was $\sim$0.″15 while at the IRTF it was $\sim$0.″36. In both cases the seeing disc is, at worst, critically sampled under good seeing conditions. The pixel scales also compare favorably with the diffraction limit at 10 μm of each telescope, 0.″84 and 0.″31 at the IRTF and Gemini, respectively. All observations were made at a resolving power $R \simeq$ 80,0000, or $\Delta v \sim$ 3-4 km s^{-1} and the spectral coverage at each spectral setting was $\Delta\lambda \approx 0.06$ μm. The spectral sampling of the TEXES array is about 1.0 km s^{-1}. Slit widths for the 2007 observations were 0.5″ at Gemini and 1.4″ at IRTF in 2001.

Spectra were obtained in "long slit" mode in which the dimensions of the slit in projection on the sky are large enough to sample the sky sufficiently for its contribution to be easily removable in data reduction. This approach eliminates the need for explicit sky pointings for sky removal. We alternated the telescope between two positions on the sky in the slit direction, separated by $\sim$ 1-5″, during an exposure sequence. Subtraction of adjacent "nod" positions removes the contribution to the signal from night sky emission. Slit lengths are determined by the length of the "nod throw", or distance between nod points, and are achieved by adjustments of counterrotating slit and decker

wheels.

To correct for absorption by the Earth's atmosphere we observed objects whose spectra were close to blackbody over the wavelength range of observation. At wavelengths beyond ~ 8 μm, asteroids meet this requirement while providing the most flux of available object types. Toward 5 μm, most asteroids provide insufficient flux to achieve high signal-to-noise ratio (S/N), so we frequently used bright, hot Main Sequence stars such as Vega (α Lyrae), Fomalhaut (α Piscis Austrini) and Mirfak (α Persei) as divisors. We aimed to observe the divisor for a given object at nearly the same airmass as the object observation for more complete divisions as telluric atmospheric absorption goes as the path length of the sightline through the atmosphere. Airmass differences can be corrected for after data reduction by taking either the object or divisor spectrum to the power of the ratio of airmasses, resulting in typically quite good divisions. Residual structure in divided spectra is removed by fitting and subtracting off low-order polynomials.

2.1 Data Reduction

Intense emission by the instrument, telescope and sky at the wavelengths of our observations would otherwise overwhelm the faint astronomical signals we try to detect, but these signals can be recovered with proper calibration making use of the same emission. The data reduction pipeline we used is described in detail in Lacy et al. (2002), based on the approach of calibrating millimeter and submillimeter data in sources such as Ulich & Haas (1976).

A typical sky calibration cycle involves collecting data on the sky and on with two positions of a rotating chopper blade mounted just above the entrance window to the TEXES Dewar: one painted black and one "shiny" (low emissivity). The result of taking black-sky removes atmospheric absorption and serves as both a spatial and spectral flat field image provided that the black position, sky and telescope temperatures are all approximately equal. We quote the Lacy et al. (2002) expression for the object intensity as a function of frequency,

$$I_\nu(object) \approx S_\nu(object - sky)\frac{B_\nu(T_{tel})}{S_\nu(black - sky)} \tag{2.1}$$

where S_ν is the measured signal and B_ν is the blackbody function at the telescope temperature T_{tel}. Within the approximation that I_ν(black)-I_ν(sky) = $B_\nu(T_{tel})e^{-\tau_{sky}}$, this procedure corrects for sky absorption. Wavelength calibration is achieved by using the known wavelengths of night sky emission lines.

Pipeline software written in FORTRAN performs the reduction steps resulting in a wavelength- and flux-calibrated object spectrum along with an estimate of the noise, the sky transmission spectrum, and the 2-D unextracted slit image. The program also corrects for optical distortion, removes cosmic ray spikes and fixes bad pixels. The accuracy of radiometric calibrations is $\sim$25%, ignoring telescope pointing uncertainties. Expressed in velocity units, our wavelength calibration method is accurate to about 1 km s^{-1}.

2.2 Spatial Resolution of IRS 9

Given the high spatial resolution of the Gemini observations, we considered the possibility that TEXES might resolve the emitting/absorbing region around IRS 9 if it were spatially extended. To that end we obtained spatial-spectral maps of IRS 9 and μ Cephei, a mid-infrared-bright standard star that was used as a PSF reference for spatial deconvolution. To generate the maps, the TEXES slit is stepped across an object and spectral information gathered at each step, building up a data cube in which there are two spatial dimensions and one spectral dimension. Additional steps are included at both the beginning and end of the scan to sample the sky for removal. The data are handled by our reduction pipeline in a manner substantially similar to the method of processing the long slit observations, treating a scan as a series of 2-D spectrograms and resulting in a calibrated data cube as output.

IRS 9 and μ Cep were observed with identical scan parameters including scan direction, length and step size, and were observed at comparable zenith angle. After reducing the raw data, different spectral windows were selected from which to form reconstructed images of each object by summing the data in the spectral direction. For IRS 9, we chose a window centered at about 745.88 cm^{-1}, near the position of the C_2H_2 ν_5 $R(6)$ line in the rest frame of the object. The window was 0.35 cm^{-1} wide. We selected this frequency range to search for spatial extent in the IRS 9 map as we noted absorption in the $R(6)$ line in nod-mode spectra. For the deconvolution reference, we chose a nearby spectral region apparently free from telluric and stellar photospheric

absorption centered at 744.43 cm^{-1} and 0.25 cm^{-1} in width. The observed full width at half maximum (FWHM) for each object was 0.″67 for IRS 9 and 0.″63 for μ Cep, at each object's respective spectral setting. The deconvolution was performed using the maximum entropy method (Bryan & Skilling 1980), with results shown in Figure 2.1. The deconvolved image of IRS 9 in the C_2H_2

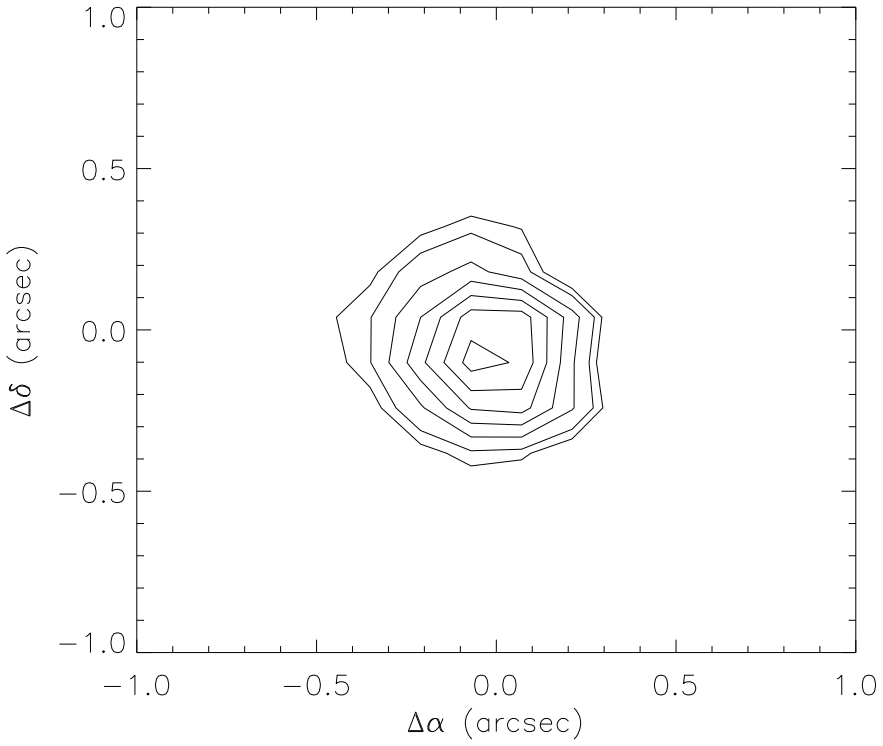

Figure 2.1 Contour plot of the TEXES scan map of NGC 7538 IRS 9 at 745.8 cm^{-1} after maximum entropy deconvolution. The PSF reference for the deconvolution was a scan map of the mid-infrared standard μ Cephei made with the same parameters as the IRS 9 scan. North is up and east at left and contours are plotted at flux densities of 25, 50, 100, 150, 200, 250 and 300 Jy. The plot origin is approximately the location of the source peak intensity.

feature appears pointlike with some weak extension toward the NE possible. We do not believe this indicates that the envelope or other structure of IRS 9 is spatially resolved, and carried out our other TEXES observations exclusively in long slit mode.

This approach to deconvolution involves some caveats. Poor seeing during a scan, for example, might distort the PSF on time scales shorter than those required to scan across an object. However, we felt sufficiently convinced that IRS 9 presents itself as a point source in the mid-infrared that we did no further scans. Given the distance to NGC 7538 and the spatial resolution of our observations, we conclude that spatial structure of IRS 9 is unresolved on scales of $\sim$1000 Astronomical Units (AU) or about 10^{16} cm.

Chapter 3

Description of the Data

The reduced data are organized into files containing one spectral setting apiece, with each setting consisting of several individual echelon orders. A sample reduced spectrum is shown in Figure 3.1. Various dropouts in the spectrum are caused by gaps between the cross-dispersed spectral orders and regions of strong atmospheric absorption. In both cases, the data values have been set to zero such that division by a telluric divisor does not yield excessively large data values. There is also some residual absorption from atmospheric features left after division such as the weak lines around 743.2 cm^{-1} in the figure.

We observed IRS 9 in the lines of seven molecules at the settings summarized in Table 2.1. The selection of settings to observe was motivated by the desire to include as many species and individual lines as possible given the severity of telluric atmospheric absorption at a particular setting. In particular, variations in the H_2O column over Mauna Kea often influenced the settings observed on a particular night, as many of our settings are sensitive to the intensities of telluric water lines. The systemic velocity of IRS 9 and motion of the Earth with respect to the LSR were taken into account in choos-

ing settings in which certain lines were shifted either into or away from nearby telluric absorption features, and in many cases required trade-offs in order maximize efficiency and scientific return.

Details of the observations for specific molecules follow. Plots of individual spectral features along with model spectra are shown in Figure 4.1 through 4.8 in Chapter 4. In Section 4.1.3 we set upper limits on the column densities of molecules in cases where their lines were non-detections in our spectra.

3.1 C_2H_2

At Gemini, two lines in the acetylene ν_5 R branch were observed (J=5 and 6), along with approximately ten lines in the ν_5 Q branch; Figure 3.2 shows the Q branch spectrum along with a simple LTE fit at a single excitation temperature. Each acetylene line appears to consist of a single component. The $R(5)$ line is stronger than $R(6)$, as is expected due to its three times greater nuclear statistical weight. $R(6)$ appears to have a weak redshifted emission component at an LSR velocity of -54 km s^{-1} although this effect may in fact be due to a poor fit to the continuum there.

Earlier IRTF observations of the ν_5 $R(1)$ line (wavenumber center 734 cm^{-1}) in 2001 June revealed a positive detection, but more importantly, higher J settings R(15,16) (768 cm^{-1}) and R(21,22) (780 cm^{-1}) were clear non-detections. The latter setting included the $^2P_{1/2} \rightarrow {}^2P_{3/2}$ fine structure line of [Ne II]; consistent with the weak free-free emission observed toward IRS 9,

this line was also a non-detection. Finally, although the positions of lines of $^{13}C^{12}CH_2$ fell in some of our spectral settings, we did not detect any lines of this isotopologue of acetylene.

We also did not detect any lines in the $2\nu_5$-ν_5 "hot band" of acetylene toward IRS 9. A cluster of hot band Q-branch lines near 731 cm^{-1} forms a band head that might have been detectable even if the individual lines were weak, but this feature was Doppler shifted out of the spectral window for the setting including the ν_5 Q branch. Other lines within the setting are subject to contamination by ν_5 lines. The hot band Q branch was seen toward IRS 1 (Knez et al. 2008), and its absence in the spectrum of IRS 9 in part leads us to conclude for the purpose of our analysis (Chapter 4) that there is little to no population of the excited vibrational states of C_2H_2.

The presence of $\nu_4+\nu_5$ combination mode lines in our spectra, shown in Figure 4.2, is of particular interest. A C_2H_2 molecule in the ground vibrational state can be radiatively excited to this mode by absorption of a photon at 7.6 μm, but there are no allowed transitions to this mode from the ν_5 mode. The only other way to excite the $\nu_4 + \nu_5$ mode is by an upward radiative transition from ν_4 at 13 μm; conversely, an acetylene molecule in the combination mode can radiatively decay to ν_4. However, there are no allowed radiative transitions from ground to ν_4, so the population of molecules in this mode is determined largely by collisions (and hence, temperature) and the population of the combination mode. Overpopulation of ν_4 may occur if densities are low enough such that collisional de-excitation of the mode occurs more slowly

than radiative decay of the combination mode. Three P-branch lines ($1 \leq J \leq 3$) of the $\nu_4 + \nu_5$ mode fell within the spectral setting centered at 1323 cm^{-1}. Of these, $P(2)$ and $P(3)$ are unambiguous detections. The $P(1)$ line is an apparent non-detection as its Doppler-shifted wavenumber center fell on a telluric atmospheric feature that did not divide out well. The ratio of the strengths of $P(3)$ and $P(2)$ is not quite 3:1 for the reason stated above, probably indicating saturation of the lines. In particular, these lines may result from absorption in a component with a small covering factor that is strongly saturated. The shapes of the detected $\nu_4 + \nu_5$ lines are rather different than those in the ν_5 R branch, being more asymmetric with a blue wing extending off to nearly -90 km s^{-1}. In fact, we note that the -80 km s^{-1} component of these lines is consistent with the velocity of the main absorption component of CO (Section 3.5) toward IRS 9, and the shape of the two lines' blue wings is similar. This may indicate the presence of combination-band C_2H_2 in the same outflow that CO is known to trace.

3.2 HCN

Two of our spectral settings contained R-branch lines of the ν_2 mode of HCN, with centers at 734 cm^{-1} ($6 \leq J \leq 7$) and 761 cm^{-1} (J=16). The $R(6)$ line fell into a region where atmospheric transmission is not favorable, and $R(7)$ appears to be a marginal detection because of a weaker, nearby atmospheric feature. $R(16)$ falls close to the $R(13)$ line of C_2H_2 but is sufficiently separated from the acetylene line to prevent blending and is the only clean HCN line

detected. This line is shown in Figure 4.2. The rest frequency of the $R(15)$ line of HCN falls outside the spectral window of the 761 cm^{-1} setting but the combination of the systemic velocity of NGC 7538 and the motion of the Earth toward the LSR at the time of observation shifts $R(15)$ just inside the first echelle order of the setting. While the noise rises rapidly toward the edge of the order, $R(15)$ is a tentative detection. The S/N of the HCN observations is generally lower than that of C_2H_2 ν_5 R branch, but the HCN lines are clearly the broader of the two. The mean FWHM of the four R-branch lines is $\sim$6.5$\pm$1 km s^{-1}, whereas the HCN $R(16)$ line FWHM $\sim$ 15 km s^{-1}. Finally, lines of the $H^{13}CN$ isotopologues are also found in these settings: $R(9)$ in 734 cm^{-1} and $R(18)$ in 761 cm^{-1}. $R(18)$ falls into a gap between orders and $R(9)$ was affected by poor atmospheric transmission.

3.3 CH_4

We obtained data on three R-branch lines of ν_4 $^{12}CH_4$: the $R(0)$ line at 1311.43 cm^{-1} and the two $R(2)$ lines at 1322.083 cm^{-1} and 1322.152 cm^{-1}. In addition, the settings for these lines contained the positions of the $R(1)$ and $R(4)$ lines of $^{13}CH_4$, but both of these lines were clear non-detections. The $^{12}CH_4$ lines show clear asymmetries indicative of multiple components. Each feature has a principal component corresponding to greatest absorption at v_{LSR} = -65.0 km s^{-1} with additional components on the red wing of this feature separated in velocity by up to 6.5 km s^{-1}. Samples of the spectra are shown in Figure 3.3.

3.4 NH_3

Two spectral settings observed contain a total of ten lines of $^{14}NH_3$, three in the ν_2 antisymmetric $P(4,K)$ states and seven in the ν_2 symmetric $P(7,K)$ states. Of the possible lines in these settings, only a$P(4,2)$ was not observed because of its proximity to a strong telluric atmospheric feature. Almost all of the NH_3 lines share a characteristic P Cygni profile, with an emission peak near the systemic velocity, around -60 km s^{-1}, and weak blueshifted absorption separated in velocity by 2.5 to 10 km s^{-1}. This may be compared to the -56.5 and -59.8 km s^{-1} absorption components seen in mid-infrared NH_3 absorption transitions toward IRS 1 by Knez et al. (2008) and a value of -60.0 km s^{-1} for the (3,3) rotational transition of NH_3 in Very Large Array (VLA) observations of IRS 1 at centimeter wavelengths (Henkel et al. 1984). The degree of absorption toward IRS 9 relative to emission varies as well; the highest K lines in the s$P(7,K)$ series appear to show no absorption at all despite the fair S/N of the data. Finally, we observed a setting near 930 cm^{-1} containing the positions of the ν_2 antisymmetric Q-branch lines ($1 \leq J \leq 9$); the data show weak absorption features at some of the indicated points. The data are shown in Figure 3.4. For comparison, a similar plot of the symmetric $P(7,K)$ branch spectrum is also shown in the figure. We did not observe lines in the ν_2 R-branch of NH_3 because of their proximity to regions of significant telluric atmospheric absorption. The R-branch lines are also located in a spectral region of rapidly increasing absorption due to the 9.7 μm silicate dust feature.

The observed pattern of absorption and emission between the ammonia

Q- and P-branches is an unexpected result, given a picture of the envelope of IRS 9 in which pure absorption of light dominates the radiative transfer. In Section 4.3 we present a physical scenario that qualitatively explains our observations, along with some calculations suggesting quantitative plausibility.

3.5 CO

We observed two settings in the 5 μm v = 0-1 band of CO which included a number of P-branch lines of several isotopologues. These settings were centered approximately at 2055 cm^{-1} and 2085 cm^{-1}. Strongest among the features were the ^{12}CO lines with J = 14, 15, 21 and 22. Each line exhibits strong P Cygni profiles with emission and absorption components separated by $\sim$20 km s^{-1}. Each component was broader than those of any line of any other molecular species we observed, with linewidths near 10 km s^{-1}. In each case the strength of the emission was approximately equal to the strength of the absorption. The features are consistent with an expansion or outflow and have been previously interpreted as an outflow by Mitchell & Hasegawa (1991). Observations of IRS 1 were also made at these settings; we find a different profile altogether with a double-bottomed absorption feature in ^{12}CO, weaker absorption on the blue wing and a slight emission bump on the red wing of each feature.

Four corresponding ^{13}CO P-branch lines with J = 3, 4, 11 and 12 were also detected in the spectrum of IRS 9. Of these, $P(11)$ was a clear detection near the middle of a spectral order and away from contamination by telluric

atmospheric lines, $P(12)$ was noisy and found very near the edge of a spectral order, and $P(8)$ and $P(9)$ blended slightly with two nearby $C^{18}O$ features. Additional ^{13}CO lines, $P(11)$ and $P(12)$, are located in the spectral setting at 2055 cm^{-1} but occur in regions of strong telluric atmospheric absorption and thus were not detected. We also searched for lines attributable to $C^{17}O$ but did not confidently detect any; this not surprising given the low abundance of $C^{17}O$ in disks. For reference, Smith et al. (2007) quote $C^{16}O$ / $C^{17}O \sim 2700$ toward the young stellar object VV CrA, obtained at a spectral resolution similar to our TEXES observations. Given the relative weakness of the $C^{18}O$ lines, it is not surprising that we did not see any features attributable to $C^{17}O$.

The CO lines seen toward both IRS 9 and IRS 1 have different line shapes in ^{12}CO and ^{13}CO. In the case of IRS 1, the ^{13}CO features show only single components in the deepest absorption, while toward IRS 9 the ^{13}CO $P(11)$ line and ^{12}CO lines show the pronounced P Cygni profiles. The spectra of both objects are plotted in Figure 3.5. The ^{13}CO lines in the 2085 cm^{-1} setting clearly show multiple components suggestive of P Cygni profiles in which emission is weak relative to absorption, and there are at least two distinct absorption units. In turn, the strongest absorption components show weak double-bottomed structure like the ^{12}CO lines in IRS 1. The multiple absorption units may appear in the profiles of the ^{12}CO features in the same spectral setting; weak "shoulders" on the blue wing of the absorption component are consistent with additional absorption components suffering contamination by the primary components. Such shoulders are also noticeable on the red wings

of the emission features of ^{12}CO . These details can be seen in Figure 3.6.

The detection of ^{13}CO toward IRS 9 at a column density comparable to those derived from spectra of ^{12}CO strongly indicates saturation of both isotopologues. Useful columns may however be obtained from rarer variants such as C^{18}O. It would also be of interest measure the ^{12}C/^{13}C ratio toward IRS 9 for comparison with the value of 45 toward IRS 1 reported by Knez et al. (2008). As we did not observe the ^{13}C isotopologues of C_2H_2 and in our spectra of IRS 9, the CO observations may offer a way to measure the ratio.

3.6 OCS

Carbonyl sulfide (OCS) is a molecule that commonly occurs in ices along sightlines through molecular clouds; Tielens (2005) cites an OCS ice abundance of 0.1% relative to H_2O ice toward IRS 9 given a water ice column density of 1×10^{19} cm^{-2}. That figure may be compared to an ice abundance of 10% for all forms of CO. In interstellar ices, OCS is commonly found in association with hydrogenated species such as H_2O and CH_3OH (Palumbo et al. 1997; Dartois et al. 1999). Laboratory results reported by Collings et al. (2004) indicate that OCS in a H_2O mixture desorbs at $\sim$150 K, implying that significant columns of this molecule may not exist in cold envelopes. However, C_2H_2 is seen toward IRS 1 and IRS 9, for example, and according to the same study desorbs at a slightly lower temperature. The relative columns of OCS and C_2H_2 may then reflect real differences in their abundances rather than their desorption temperatures. Knez et al. (2008) speculate that OCS should

be observable toward IRS 9 as indicated in some chemical models.

The ^{12}CO setting at 2055 cm^{-1} we observed also contains the positions of a number of P-branch lines of the ν_2 mode of OCS ($12 \leq J \leq 22$), but we cannot confidently claim detections of any of them. Periodic structure in the continuum of our 5μm spectra may be OCS features, although it is more likely the structure results from bad flat-fielding. For reference, we have overplotted the locations of the OCS line centers in Figure 3.7. It is unclear whether we should have observed lines of OCS in the gas phase, given the strong detections of CO nearby. Low temperatures may inhibit desorption of OCS from grains, but the hypothetical grounds for predicting OCS abundances are questionable: as Doty et al. (2004) point out, "In the case of OCS, the chemistry is uncertain." The signature of an outflow in the spectra of CO hints at excitation likely through shocks. We might expect that OCS would be similarly excited but there is no support for this at present.

3.7 HNCO

The occurrence of interstellar isocyanic acid (HNCO) appears to be tied to the presence of the cyanate ion (OCN^-) in which OCN^- is formed on grains by irradiation of solid HNCO in ices by UV in the presence of NH_3 (van Broekhuizen et al. 2004a). Once evaporated from grains, OCN^- may then undergo hydrogenation to become HNCO. Knez et al. (2008) observed dozens of HNCO lines toward IRS 1 and infer a column density of 5.4×10^{15} cm^{-2}; this and the value of other gas parameters from their spectra lead them

to conclude that "...gas-phase HNCO is possibly coming from evaporation of grain mantles" by way of OCN^-. A low column density compared to the value expected from the observed abundance of OCN^- is interpreted as evidence that only a fraction of the available OCN^- desorbed from grains becomes HNCO, the remainder forming other molecules in gas-phase chemistry. Interpretation of observations is difficult, however, as Knez et al. point out that chemical models do not currently include HNCO in their networks.

We looked for ν_4 mode HNCO IL-0 P-branch lines toward IRS 9 in the TEXES spectral setting that included (7,K) lines in the symmetric P branch of $^{14}NH_3$. Each of the three lines included in this setting ($2 \leq J \leq 4$) was a firm non-detection. Given the strong observed ice absorption at 4.62 μm toward IRS 9 (Pendleton et al. 1999; now commonly attributed to OCN^-) and a lack of gas-phase HNCO absorption, it seems most likely that temperatures in the outer envelope of IRS 9 are sufficiently low to prevent OCN^- desorbing from grains at any detectable rate. Alternately, gas-phase OCN^- might exist at H (or H_2) abundances insufficient to result in considerable HNCO production.

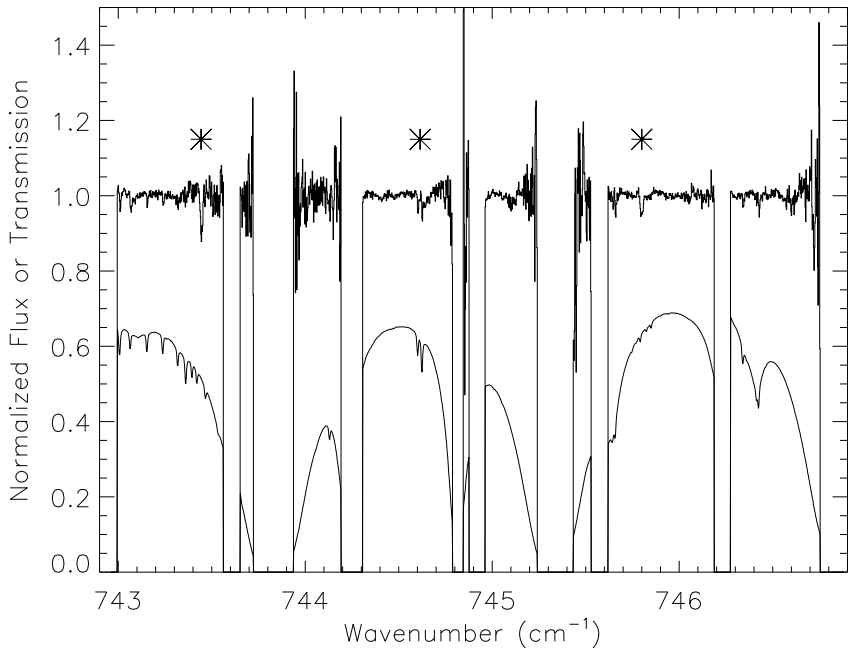

Figure 3.1 The normalized TEXES spectrum centered approximately at 744.8 cm^{-1} toward NGC 7538 IRS 9 obtained on UT 2007 October 21 at Gemini North is shown in the upper trace. The asterisks mark positions of the following features, left to right: C_2H_2 ν_5 $R(5)$, HCN ν_2 $R(10)$, and C_2H_2 ν_5 $R(6)$. Atmospheric transmission is represented by the lower trace on the same scale. The wavenumber scale has been corrected for the Earth's motion with respect to the LSR.

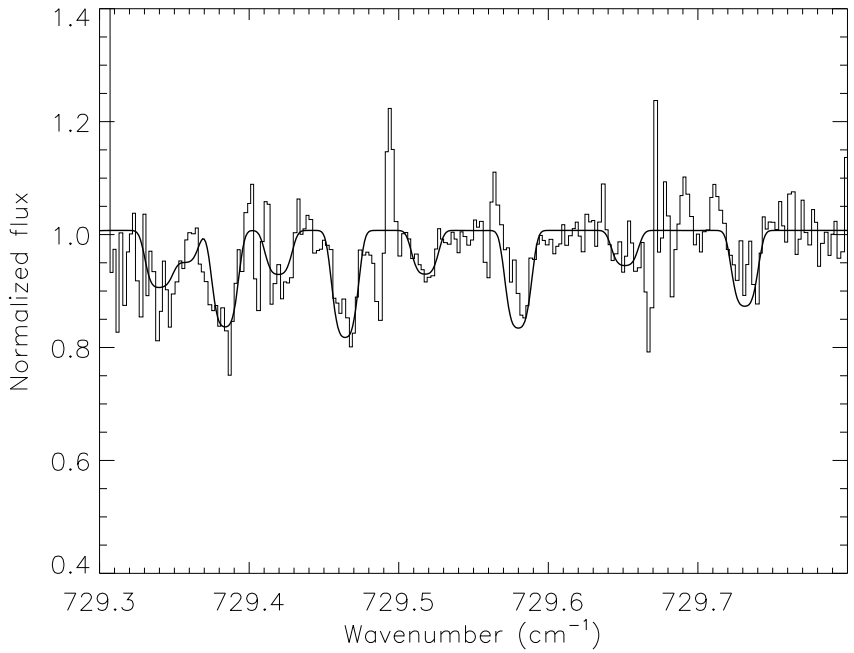

Figure 3.2 Spectrum of the ν_5 Q branch of C_2H_2 observed with TEXES toward NGC 7538 IRS 9 (thin lines). A fit is superimposed from an LTE model with $T = 100$ K, $b = 1$ km s^{-1}, and $N(C_2H_2) = 2 \times 10^{15}$ cm $^{-2}$ (thick lines). The synthetic spectrum has been convolved with the TEXES instrumental lineshape function.

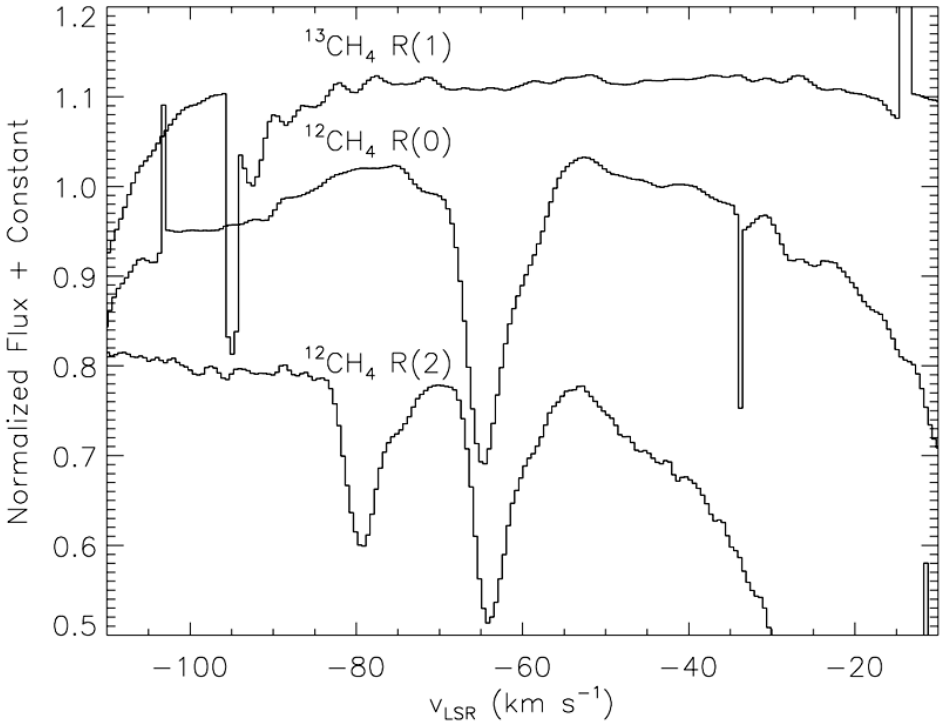

Figure 3.3 Spectra of three features in the ν_4 band of CH_4 toward IRS 9, shown on an LSR velocity scale as labeled. For the spectrum containing the $R(2)$ lines, the velocity scale has been set to the LSR value for the stronger component (rest frequency 1322.085 cm^{-1}).

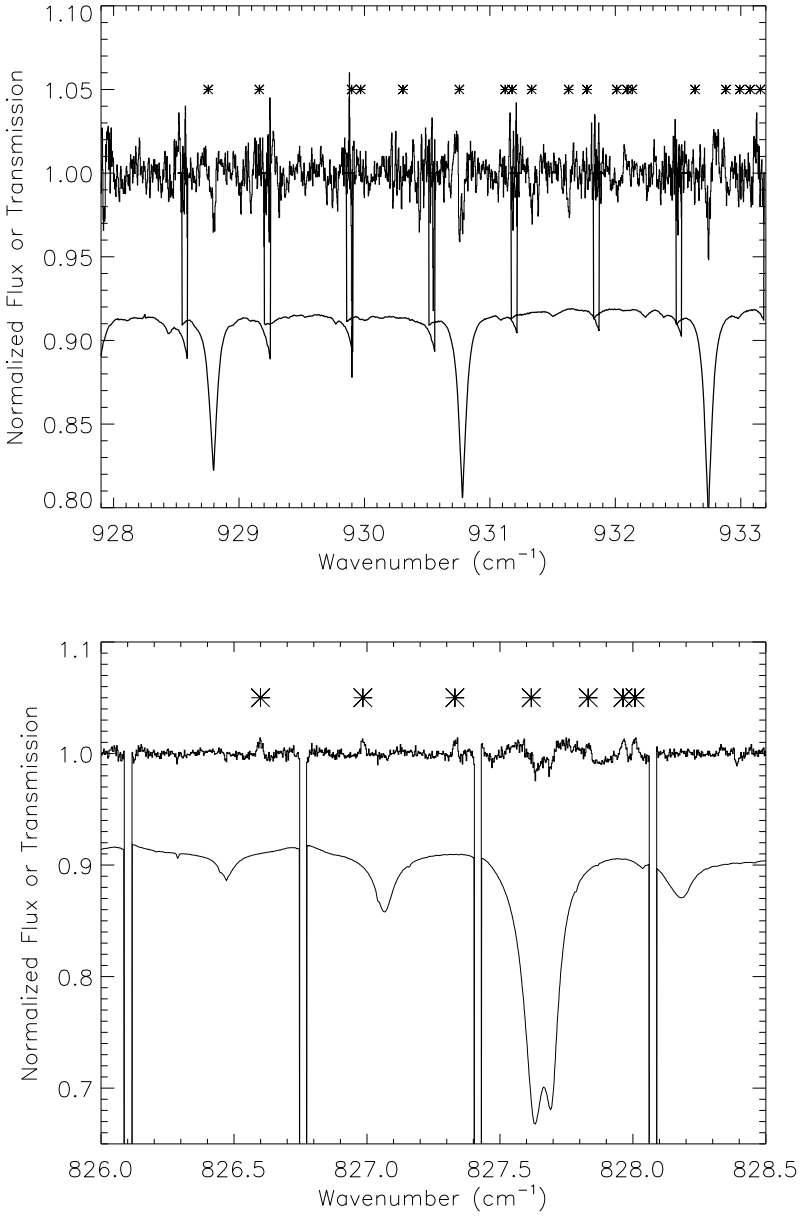

Figure 3.4 TEXES data toward NGC 7538 IRS 9 at the position of the $^{14}NH_3$ ν_2 antisymmetric Q branch (top panel) and symmetric $P(7,K)$ branch (bottom panel). The upper curve in each plot shows the data, while the lower curve in each shows the relative atmospheric transmission on the same scale. Asterisks mark positions of the NH_3 lines. Both spectra have been corrected for the Earth's motion relative to the LSR, and the position of the NH_3 lines shifted to the systemic LSR velocity of approximately -60 km s^{-1}.

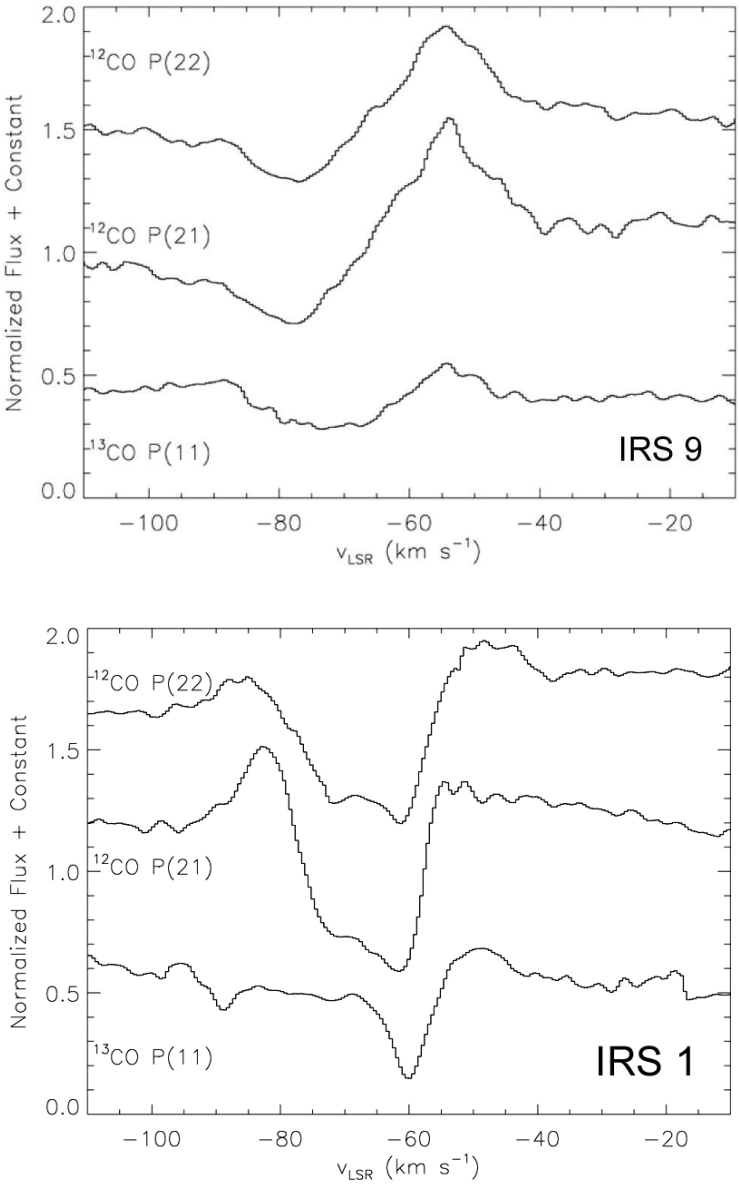

Figure 3.5 The upper panel shows spectra of two P-branch lines of ^{12}CO and one P-branch line of ^{13}CO toward IRS 9 obtained with TEXES. The lower panel shows the same spectral settings observed toward IRS 1. In both cases the motion of the Earth with respect to the LSR has been removed from the velocity scales.

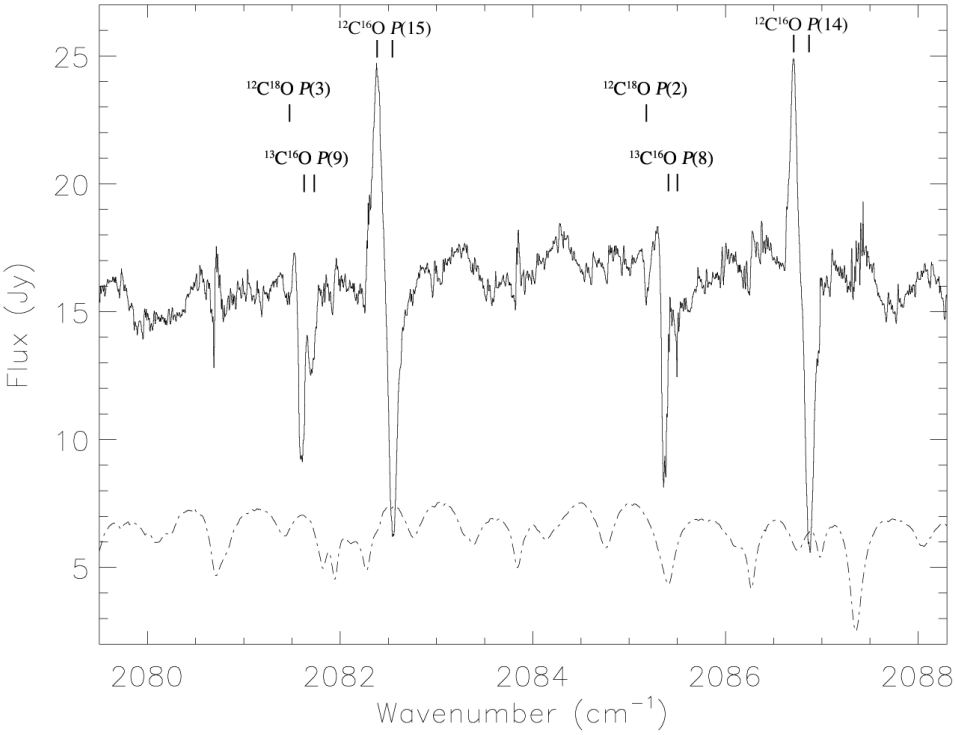

Figure 3.6 TEXES spectrum toward NGC 7538 IRS 9 centered near the 5 μm rotational lines of several isotopologues of CO. The data are shown in the upper trace (solid line) and the relative atmospheric transmission in the lower trace (dot-dashed line), multiplied by a factor of 10. Some line identifications are shown.

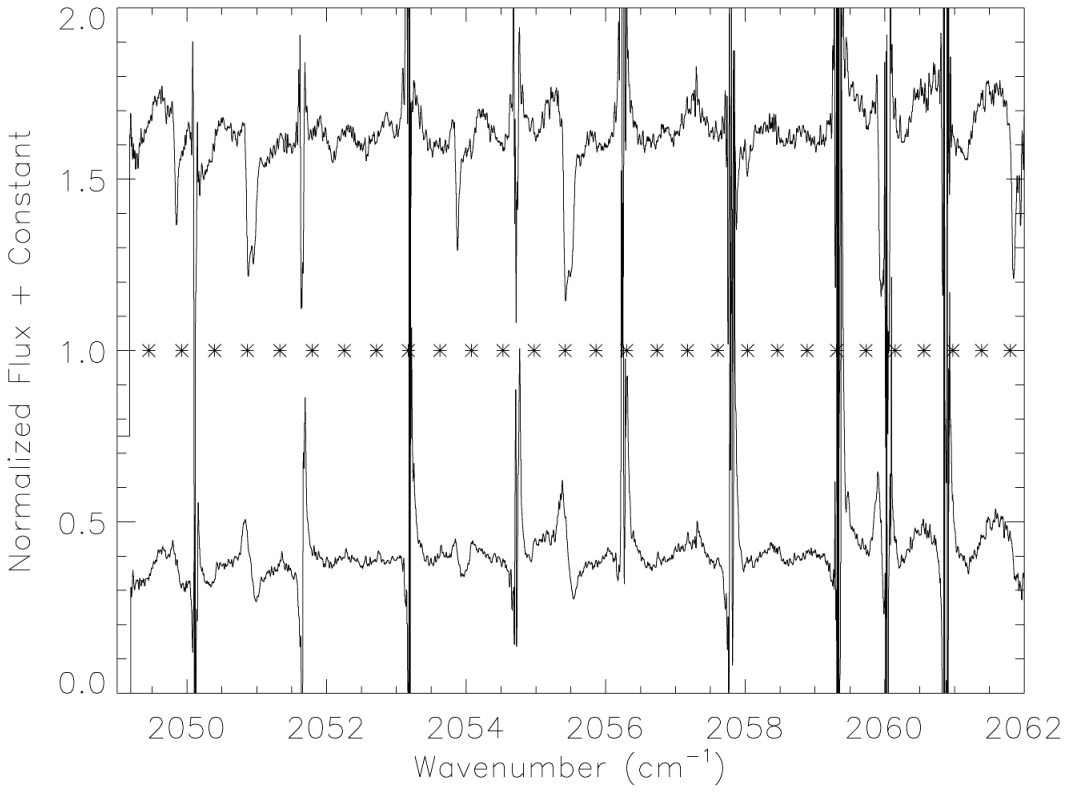

Figure 3.7 The TEXES spectra of NGC 7538 IRS 1(top) and IRS 9 (bottom) near features in the P-branches of ^{12}CO and ^{13}CO. The wavenumber scale has been corrected to a velocity reference at rest in each object's frame. Line centers of OCS features in this spectral window are marked with asterisks. The periodic regions of strong noise are due to absorption by telluric atmospheric CO_2.

Chapter 4

Analysis

Spectroscopic data can yield a wide range of information based on simple analyses of spectral lines. In the spectra of molecules, line depth, shape, and width are sensitive to the column density of molecules, excitation temperature, and turbulent broadening in the local medium, among other factors. Spectra can in turn provide useful information about the physical conditions in the media through which light passes. Our TEXES spectra of the two sources in NGC 7538 can be used to obtain information on the physical conditions in the envelope of IRS 9 and compare the results to conditions around IRS 1 found previously. First, we fit simple multi-component Gaussian profiles to spectral lines assuming pure absorption by various molecular species in local thermodynamic equilibrium (LTE) with the surrounding envelope. Some of the results were checked against a fit to the 13 μm data using χ^2 minimization fitting, with the excitation parameters of the absorbing/emitting gas as free parameters. For lines we did not detect, column density upper limits were calculated for the corresponding molecular species. The particular case of the non-detection of the 12.8 μm [Ne II] feature was useful to establish an upper limit to the ionizing flux associated with the embedded continuum source in IRS 9. Finally, we present a radiative transfer mechanism to explain the

pattern of emission and absorption lines of the ν_2 mode of NH_3 seen in our spectra

4.1 Spectral Line Fitting

We fit synthetic spectra to the TEXES data to derive excitation parameters and column densities for the various molecular species observed. A two-step process was devised in which rough estimates of the parameters were made from fits of synthetic spectra to our data; these values were then used as the initial guesses in our fitting program which iterated values of hundreds parameters to achieve the best fit to the data by minimizing χ^2. While our χ^2 code is robust in finding solutions even when starting far from the global minimum, convergence is achieved faster by using good initial guesses. This approach was best suited to our method of spectral analysis.

4.1.1 Simple Synthetic Spectrum Fitting

In order to get parameters for the gas-phase lines we observed, we fit synthetic spectra to the data using a fitting method commonly referred to as "chi by eye." This approach allowed us to get quick initial estimates of parameters such as excitation temperature and column density for the various molecules we observed which were then used as inputs to a more sophisticated non-linear least squares code to obtain better values for the parameters. The simple approach also allowed us to determine the number, width and velocities of line components.

The equivalent width for a given line is the product of the line strength, α and the column density, N. We obtained values of α from the GEISA database of laboratory molecular data (Jacquinet-Husson et al. 2005). The GEISA coefficients are specified for $T_o = 296$ K; we corrected them to an assumed T via the formula

$$\alpha(T) = \alpha(T_o) \exp\left[E_l \left(\frac{1}{k_B T_o} - \frac{1}{k_B T}\right)\right] \left(\frac{T_o}{T}\right)^{\beta} \tag{4.1}$$

where E_l is the energy of the lower state of a transition, k_B is Boltzmann's constant, and $\beta = 1$ for linear molecules and $\frac{3}{2}$ for non-linear molecules. This formula is valid specifically for NH_3; different exponents apply to the T_o/T term for other molecules. Here the contributions of the vibrational partition function and the stimulated emission correction are neglected as both are of order unity. For optically thin lines, the line center optical depth is calculated according to

$$\tau_l = \frac{W}{b\sqrt{\pi}} \tag{4.2}$$

where W is the line equivalent width and b is the $1/e$ half-width of the line profile, also known as the Doppler "b" parameter. The run of optical depth with frequency over the line is computed according to

$$\tau(w) = \tau_l \exp \frac{-(w - w_o)^2}{b^2} \tag{4.3}$$

in which w is the wavenumber and w_o is the line center wavenumber. The optical depths are converted to intensities by taking the exponential of $\tau(w)$ where the intensities are normalized to a maximum value of unity. We assumed the

excited vibrational states were not populated, and that the rotational states were in LTE. Our radiative transfer model assumed pure absorptions for fitting the observed absorption lines; emission lines were treated as a case of negative absorption, so the interpretation of fitted quantities such as the column density is somewhat unclear. Temperatures were not constrained in this fitting but were arbitrarily set to 200 K; this value is consistent with temperatures around IRS 1 derived from TEXES data. The exception was the Q-branch of C_2H_2 where a number of observed J states allowed the temperature to be constrained to 100 K.

The results of this fitting are shown in Figures 4.1 through 4.8, and the derived "best fit" gas parameters are collected in Table 4.1. Column densities are given as *total* column density in a given molecule rather than on a component-by-component basis. Instances of emission were treated as negative absorption, hence negative values of the column density in the table for components in emission.

4.1.2 χ^2 Minimization Spectral Fitting

Our spectral fitting code, `fitspec`, used the Levenberg-Marquardt method of inverting the second derivative matrix to minimize χ^2 as in Bevington & Robinson (2003). The 1-D radiative transfer model for our synthetic spectra assumes both rotational and vibrational LTE of all molecules as appropriate with a single excitation temperature. All other parameters are free to vary in the fit. The total number of free parameters depends on the number

Table 4.1 Molecular absorption parameters derived from simple synthetic spectrum fitting in LTE

Molecule/Band	Line	n[a]	T (K)	v_1[b] (km s^{-1})	v_2	v_3	b_1 (km s^{-1})	b_2	b_3	N_1[c] (cm^{-2})	N_2	N_3
C_2H_2 ν_5	$R(1)$	1	100	-62.0	–	–	3.3	–	–	1.0(15)	–	–
	$R(5)$	1	100	-62.0	–	–	2.4	–	–	4.5(14)	–	–
	$R(6)$	1	100	-65.5	–	–	2.4	–	–	4.5(14)	–	–
	$R(13)$	1	100	-68.5	–	–	2.8	–	–	3.0(14)	–	–
	Q branch	1	100	–	–	–	1.0	–	–	2.0(15)	–	–
C_2H_2 $\nu_4+\nu_5$	P(2)	1	100	-61.0	–	–	6.8	–	–	2.5(16)	–	–
	P(3)	1	100	-62.0	–	–	5.7	–	–	1.0(16)	–	–
HCN ν_2	$R(16)$	1	200	-64.5	–	–	7.9	–	–	1.2(16)	–	–
$^{12}CH_4$ ν_4	$R(0)$[d]	4	200	-65.0	-54.0	-61.0	2.3	2.7	4.6	7.5(16)	-4.0(15)	6.0(16)
	$R(2)$	2	200	-65.5	-61.5	–	2.3	2.5	–	6.0(16)	3.3(16)	–
	$R(2)$	–	–	–	–	–	2.5	2.3	–	6.3(16)	1.5(16)	–
$^{14}NH_3$ ν_2	a$P(4,0)$	2	200	-64.0	-70.0	–	4.6	3.9	–	-2.5(15)	5.0(14)	–
	a$P(4,1)$	2	200	-62.0	-72.0	–	5.3	3.9	–	-3.8(15)	2.5(14)	–
	a$P(4,3)$	2	200	-62.0	-70.0	–	2.8	3.9	–	-1.0(15)	1.0(15)	–
	s$P(7,0)$	2	200	-60.0	-69.0	–	2.9	2.9	–	-1.5(15)	1.2(15)	–
	s$P(7,1)$	2	200	-62.0	-70.0	–	1.8	4.0	–	-2.0(15)	7.5(14)	–
	s$P(7,2)$	2	200	-61.0	-62.5	–	3.3	2.9	–	-6.0(15)	4.5(15)	–
	s$P(7,3)$	2	200	-58.5	-64.0	–	1.8	2.9	–	-1.2(15)	1.5(15)	–
	s$P(7,4)$	2	200	-60.5	-63.0	–	1.8	1.8	–	-2.5(15)	2.0(15)	–
	s$P(7,5)$	1	200	-56.0	–	–	4.4	–	–	-7.0(15)	–	–
	s$P(7,6)$	1	200	-57.0	–	–	4.4	–	–	-4.0(15)	–	–
$^{12}C^{16}O$ v=1-0	$P(14)$	3	200	-55.0	-64.5	-88.5	2.4	6.5	7.2	-1.0(16)	-1.1(17)	3.0(17)
	$P(15)$	3	200	-51.5	-63.5	-88.5	3.6	9.4	7.2	-2.5(16)	-2.2(17)	3.0(17)
	$P(21)$	2	200	-54.5	-77.5	–	10.9	10.9	–	-8.0(17)	5.5(17)	–
	$P(22)$	2	200	-55.0	-77.0	–	8.0	10.2	–	-6.0(17)	6.0(17)	–
$^{13}C^{16}O$ v=1-0	$P(3)$	3	200	-60.5	-70.5	-89.0	4.3	4.3	1.4	-9.0(17)	8.0(18)	7.0(17)
	$P(4)$	3	200	-61.5	-71.5	-86.0	3.6	5.0	6.5	-7.0(17)	6.8(18)	3.4(18)
	$P(11)$	2	200	-54.0	-75.0	–	5.8	10.2	–	-8.0(17)	2.7(18)	–
	$P(12)$	2	200	-54.0	-73.0	–	5.9	10.2	–	-3.5(17)	6.5(18)	–
$^{12}C^{18}O$ v=1-0	$P(2)$	2	200	-68.0	-72.0	–	2.9	3.6	–	7.5(18)	7.5(18)	–
	$P(3)$	2	200	-66.0	-71.0	–	4.3	4.3	–	3.0(18)	3.0(18)	–

[a]Number of velocity components fit.

[b]All velocities are referred to the local standard of rest (LSR).

[c]Column densities are given in the form $A(B) = A\times10^B$. Negative values of A indicate components in emission.

[d]The best fit to this line required four components. The remaining component not in the table is v_4 = -71.5 km s^{-1}, b_4 = 2.3 km s^{-1}, N_4 = 5.0(15)cm^{-2}

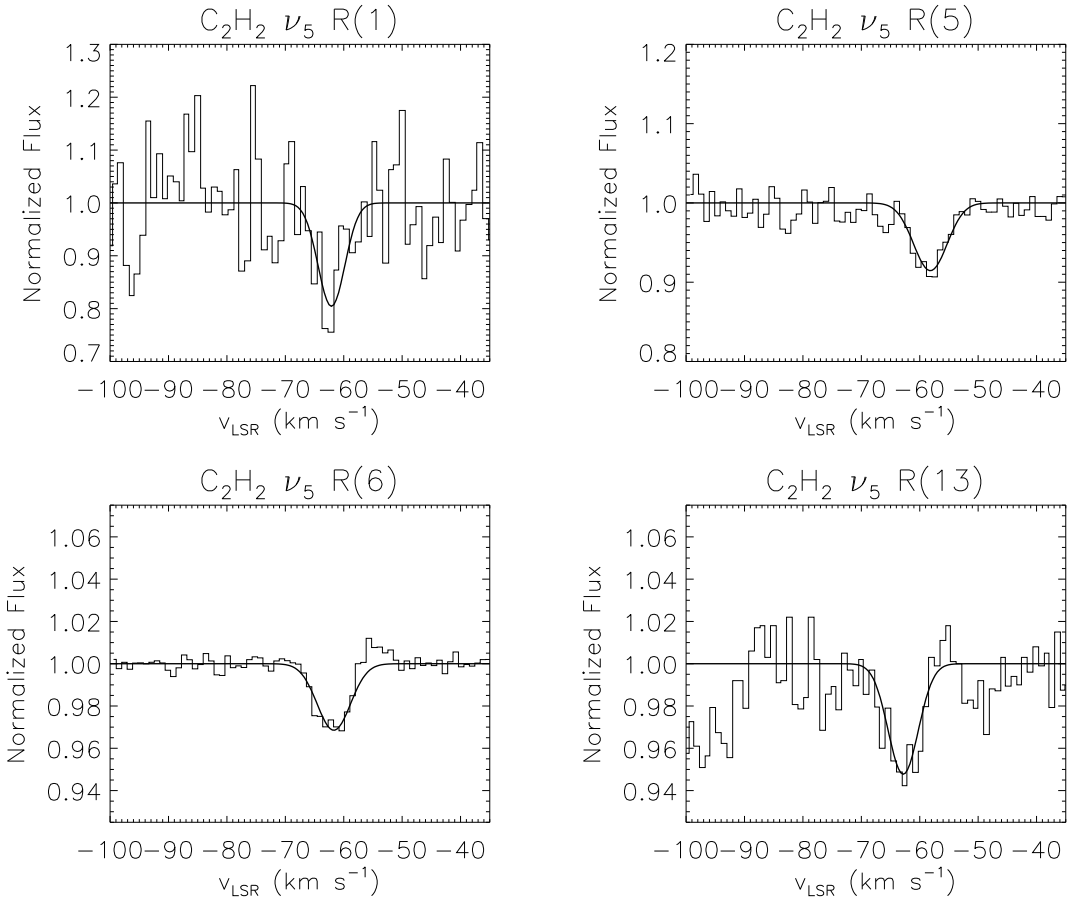

Figure 4.1 TEXES spectra of NGC 7538 IRS 9 (thin lines) and synthetic spectra obtained by the simple LTE fitting method described in Section 4.1.1 (thick lines). The continuum in each spectrum has been normalized to unity and the spectra are plotted on a velocity scale referred to the LSR. Features shown are C_2H_2 ν_5 $R(1)$, $R(5)$, $R(6)$ and $R(13)$.

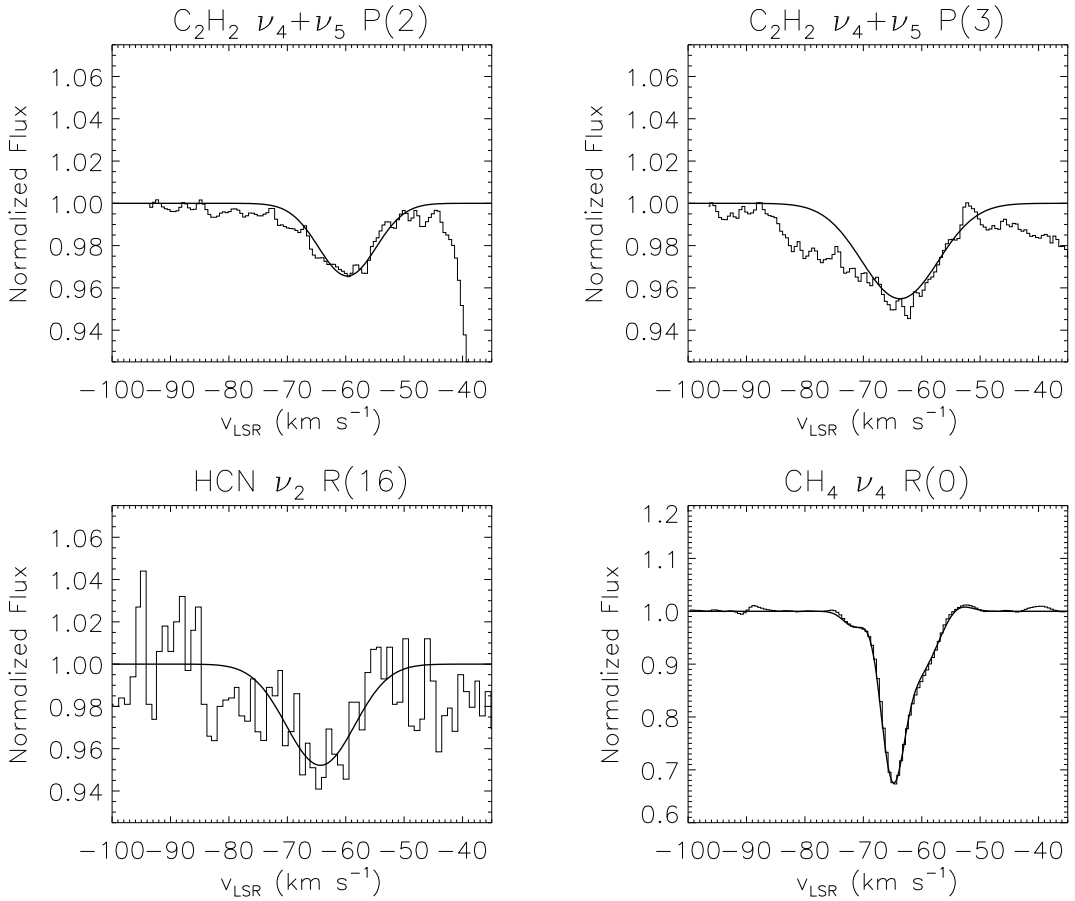

Figure 4.2 TEXES spectra of NGC 7538 IRS 9 (continued). Features shown are C_2H_2 $\nu_4 + \nu_5$ $P(2)$ and $P(3)$, HCN ν_2 $R(16)$ and CH_4 ν_4 $R(0)$.

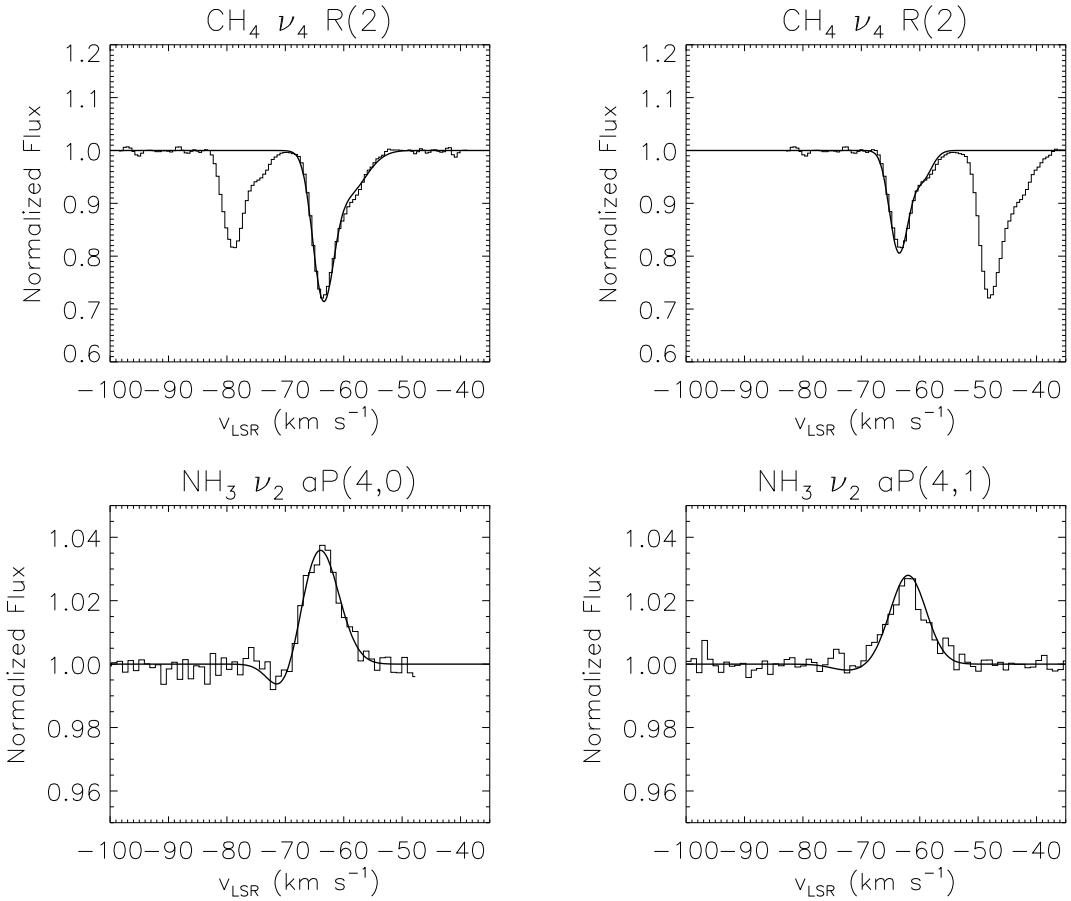

Figure 4.3 TEXES spectra of NGC 7538 IRS 9 (continued). Features shown are the two components of CH_4 ν_4 $R(2)$, NH_3 ν_2 a$P(4,0)$ and a$P(4,1)$.

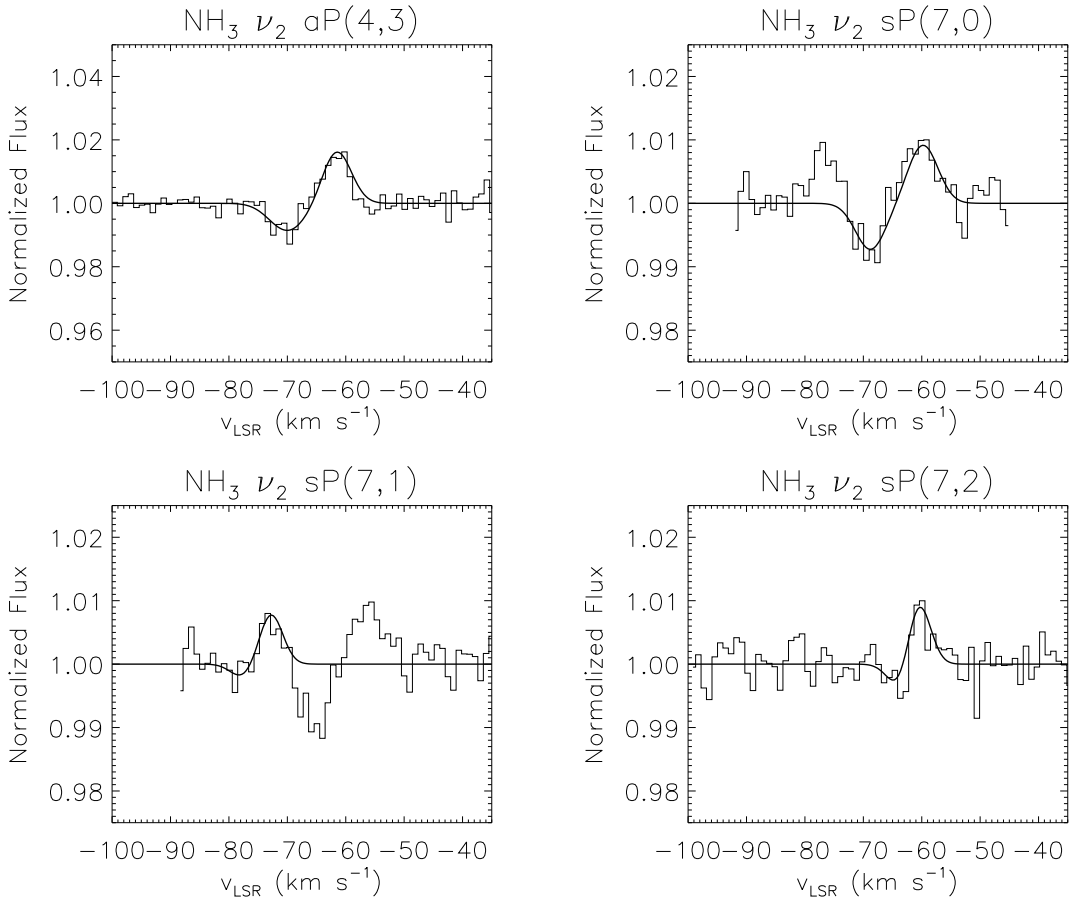

Figure 4.4 TEXES spectra of NGC 7538 IRS 9 (continued). Features shown are NH_3 ν_2 aP(4,3), sP(7,0), sP(7,1) and sP(7,2).

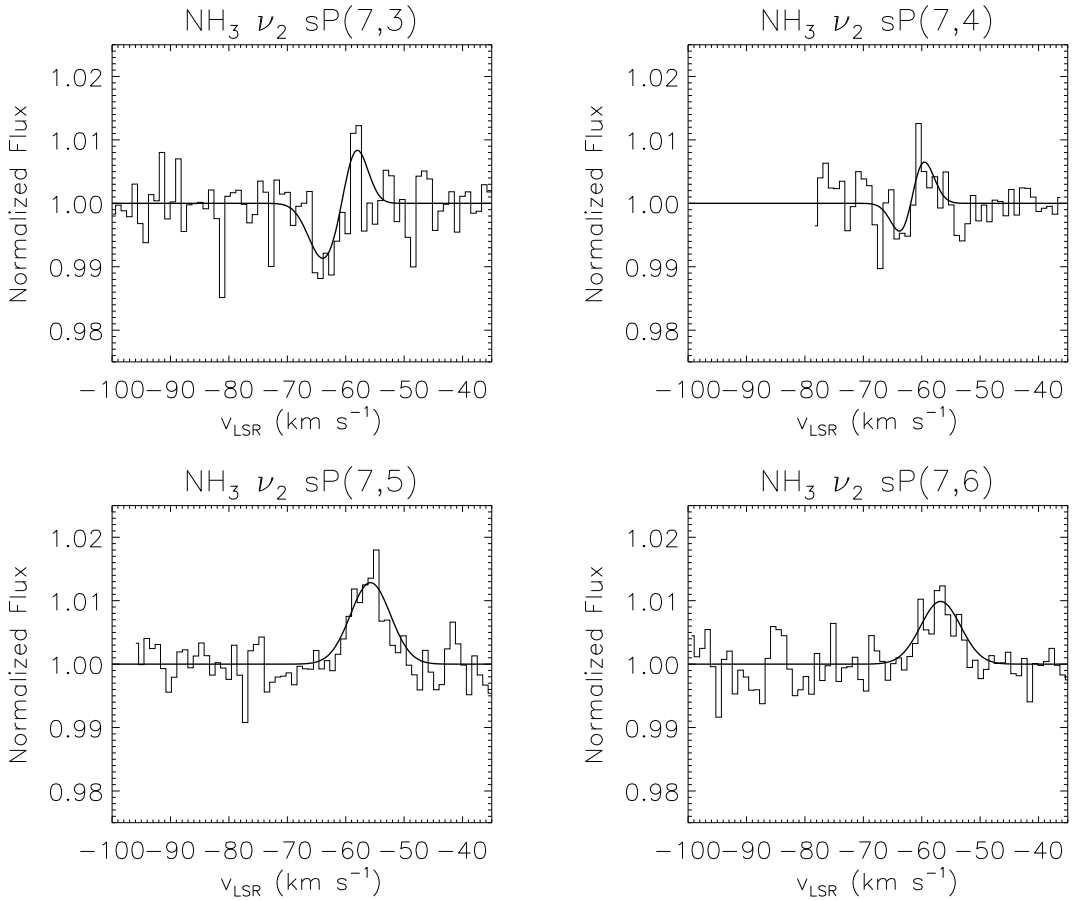

Figure 4.5 TEXES spectra of NGC 7538 IRS 9 (continued). Features shown are NH_3 ν_2 sP(7,3), sP(7,4), sP(7,5) and sP(7,6).

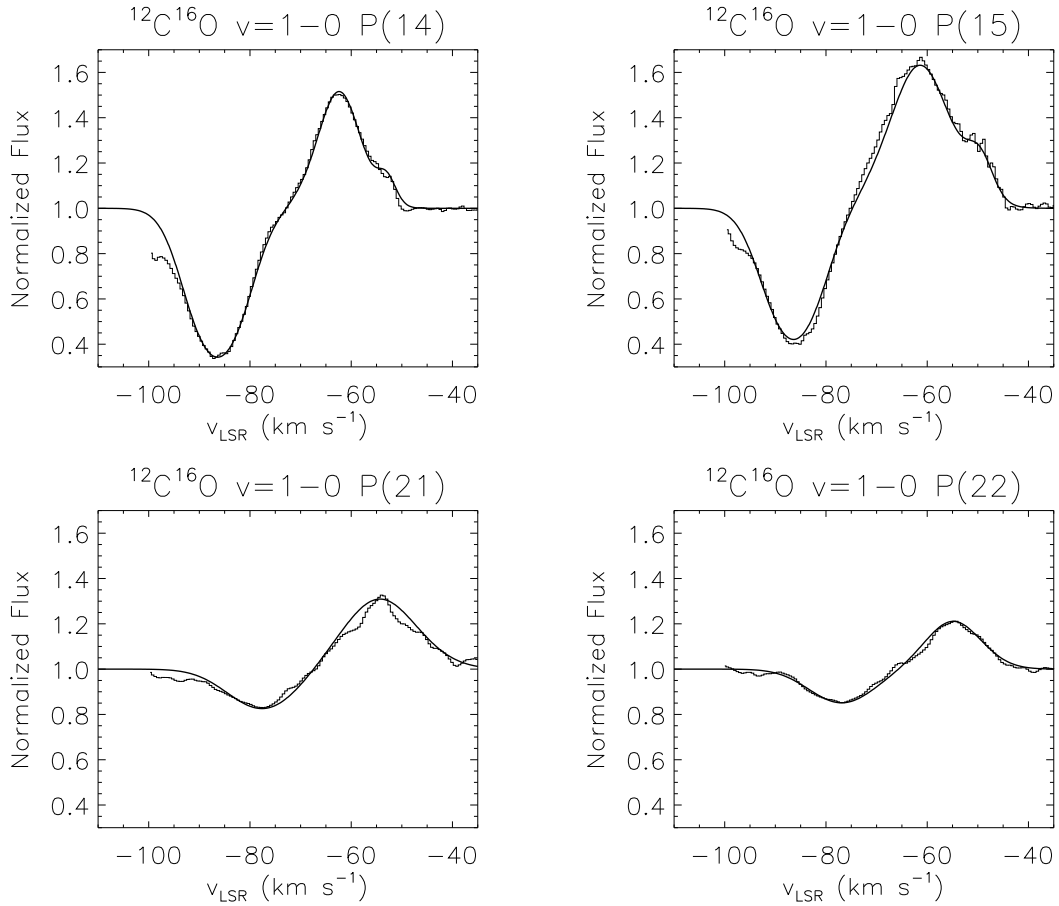

Figure 4.6 TEXES spectra of NGC 7538 IRS 9 (continued). Features shown are $^{12}C^{16}O$ v=1-0 $P(14)$, $P(15)$, $P(21)$ and $P(22)$.

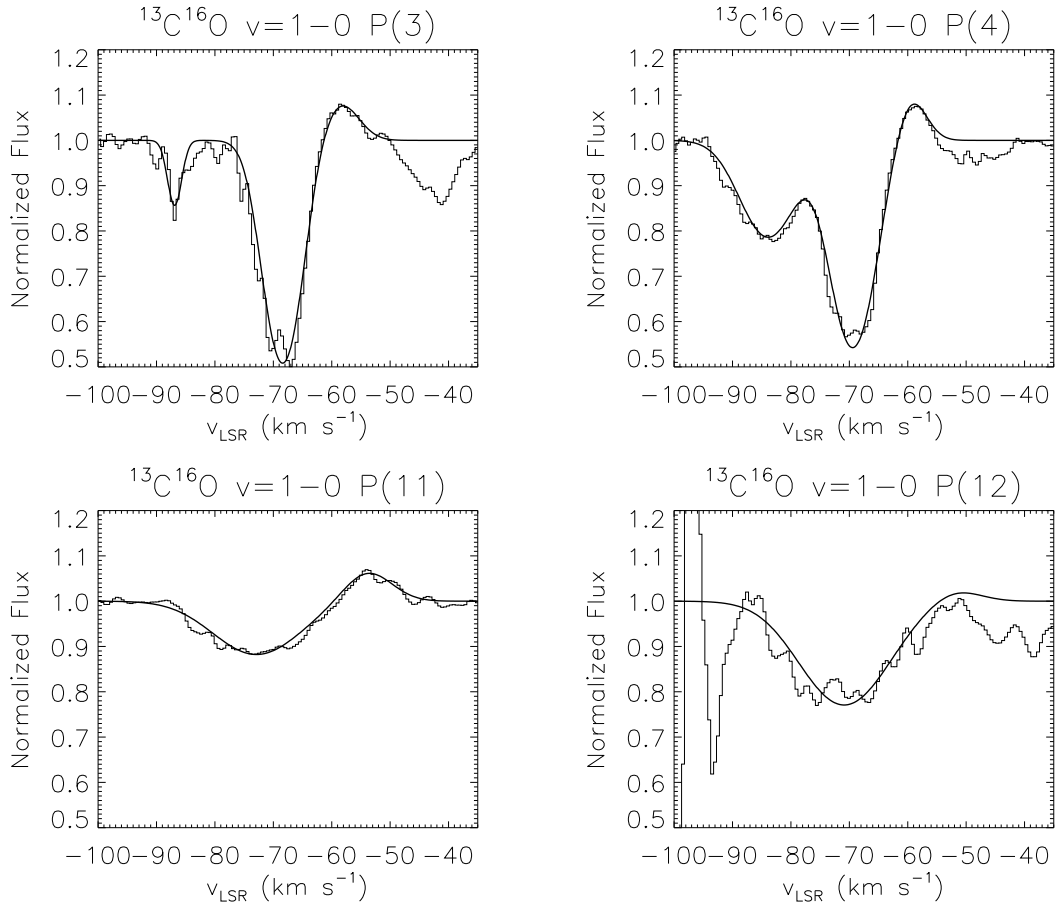

Figure 4.7 TEXES spectra of NGC 7538 IRS 9 (continued). Features shown are $^{13}C^{16}O$ v=1-0 $P(3)$, $P(4)$, $P(11)$, $P(12)$.

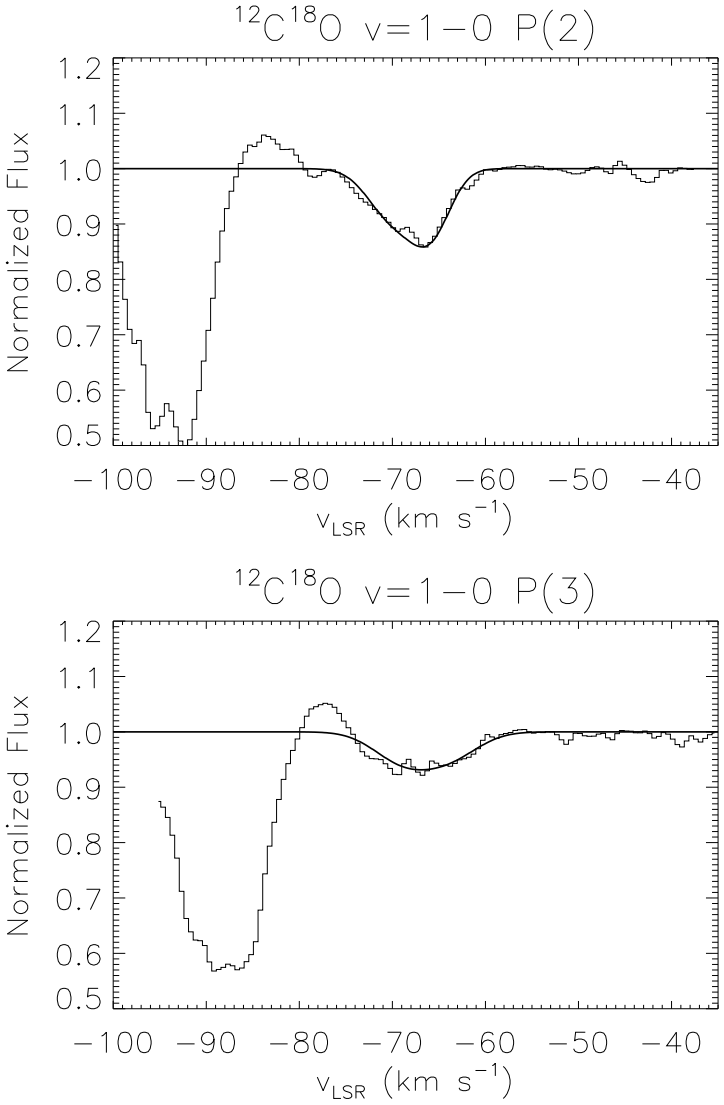

Figure 4.8 TEXES spectra of NGC 7538 IRS 9 (continued). Features shown are $^{12}C^{18}O$ v=1-0 $P(2)$ and $P(3)$.

of molecules in the fit and the number of echelon orders in a particular spectral setting.

The program can include the effects of up to four independent absorbing units, or "clouds", simply allowing their parameters to vary in the fit or holding those parameters fixed at zero to inhibit their effects. For each cloud in the model, initial values of the following parameters are specified by the user: Doppler shift (v_{LSR} in km s^{-1}), b (in km s^{-1}), the product of the covering factor and column density (in cm^{-2}), the excitation temperature (in K), and the covering factor (unitless). Here "covering factor" is understood to be the fraction of the continuum source covered by the absorbing medium. In turn, four numerical values are specified for each parameter. These are the starting value (the initial "guess"), the 1σ uncertainty in that parameter if all other parameters are held fixed, a flag that either forces the value of the parameter to be fixed or, if set to a nonzero integer N, tells the program to begin varying that parameter on the Nth iteration, and the 1σ uncertainty if all other parameters are allowed to vary. The value of parameters can be tied together if desired by setting N to be a negative number in which case it is interpreted as a *pickup*, with the absolute value of N indicating to which cloud to tie a parameter. For example, if it is presumed all clouds along the line of sight share the same systemic velocity, an initial guess for the Doppler shift need only be specified once, with the remaining clouds' velocities given as a pickup from the first value. Alternately, if the observed Doppler shift of a given spectrum were already known, it could be specified once and set to not

vary (N=0), with the other clouds' velocities given similarly. In this manner, known constraints on the fit can be built in before running the program. For each molecule, we chose a number of absorbing clouds consistent with the number of velocity components seen in the TEXES spectra, allowing `fitspec` to independently determine their velocities. When available, we included data indicating the non-detection of certain lines, such as high-J C_2H_2 near 13 μm, to better constrain the parameters of the fit.

Following the guess values for various cloud parameters are user inputs for parameters related to fitting of the continuum level in the echelle orders of each spectrum. As described previously, `fitspec` expects a continuum-normalized input spectrum and has a built-in low order fitting routine. Thus for each order in the input spectrum, the user is expected to specify the continuum level, slope, and coefficients for polynomial order up to quartic; these are adjusted iteratively along with the cloud parameters to find the best fit to the data. The orders are permitted to shift in frequency if the fit requires, although the user can override this capability by setting an appropriate flag. Finally, the success of `fitspec` requires accurate molecular transition data to compute synthetic spectra against which to fit the data. We relied on the calculations in Evans et al. (1991), giving information including line center, the energy of the transition either in units of $J(J+1)$ (which is then multiplied by the molecule's rotational constant B) or E_{lower} in units of cm^{-1}, and the rotational line strengths (Hönl-London factors) in units of cm^{-1} (10^{16} cm^{-2})$^{-1}$.

The program uses the guesses of starting parameter values to compute

the initial model spectrum, and the iterates the fit by varying those values until a convergence criterion is satisfied. The requirement is

$$\sum_i \left(\frac{p_i}{\sigma_{p_i}} \right)^2 \leq 0.01 \tag{4.4}$$

where the p_i are individual parameter values and σ_{p_i} is the uncertainty in the ith parameter allowing all other parameters to vary.

The output of the program is a file identical in structure to the input file but containing the best-fit values for the various parameters and uncertainty estimates for each. In addition, a synthetic spectrum having the properties of the best fit is generated and output as an ASCII text file for plotting. The intensity of the synthetic spectrum is calculated by taking $I = I_o e^{-\tau}$ of each absorbing unit along the line of sight as

$$I_{obs} = I_o \prod_{n=1}^{4} [1 - C_n(1 - e^{-\tau_n(\nu)})] \tag{4.5}$$

assuming all four absorbing clouds are used. In this equation, I_o is the intensity of radiation from the continuum source, C_n are the covering factors of the clouds and τ_n are the optical depths of the clouds. Knez et al. (2008) used the same approach and note that "This results in a greater absorption in saturated lines than would result if the optical depths were added first and then the transmission spectrum was calculated from the optical depth spectrum." The resulting fits to the data are better than those obtained by summing the optical depths first and then taking the exponential.

The results of our `fitspec` runs on the IRS 9 data are summarized in

Table 4.2 where they are compared with results from fitting TEXES data of IRS 1 with the same procedure in Knez et al. (2008).

4.1.3 Column Density Upper Limits For Non-Detections

We calculated upper limits on the lines that were not detected in the spectrum of IRS 9 by convolving the data with a Gaussian lineshape function whose properties were consistent with those of other, detected lines. We began by assuming a normalized spectrum containing a single absorption line has the functional form

$$F_\nu = 1 - ae^{-x^2/b^2} \tag{4.6}$$

where $a > 0$ is the depth of the line and b is the Doppler b parameter. It is convolved with a Gaussian of the form ne^{-x^2/b^2} where n is a normalization factor here chosen to be $1/\sqrt{\pi}b$ such that the area under the Gaussian is unity. The convolution is straightforward:

$$F_\nu \otimes ne^{-x^2/b^2} = \int F_\nu ne^{-x^2/b^2} d\nu, \tag{4.7}$$

where $x = \nu - \nu'$. The upper limit of the equivalent width, W, of a line not detected is proportional to the peak value of the convolved spectrum according to

$$W = \sqrt{2\pi}Pb \tag{4.8}$$

in which P is the peak and b is again the Doppler b. We used b=3.5 km s^{-1} in making the calculations, a value consistent with those derived by spectral fitting methods described previously. The column density limit for species X

Table 4.2. Molecular absorption parameters determined from χ^2 minimization spectral fitting. Quantities in parentheses are the 1σ uncertainties on the adjacent figures in the same units.

Species	v_{LSR} (km s^{-1})	T$_{ex}$ (K)	b (km s^{-1})	$N(X)$ (10^{16} cm^{-2})	C %
			IRS 9 (this work)		
C_2H_2	-64.9(0.2)	172(48)	3.2(0.5)	3.9(0.3)	10(0.6)
HCN	-58.6(0.4)	172(48)[a]	3.1(0.1)	16(4.6)	4(0.2)
NH_3	-62.0(0.1)	192(63)	2.7(0.1)	9.2(1.2)	3.2(0.2)
	-66.8(0.2)	220(60)	3.4(0.1)	1.0(0.1)	12(2)
HNCO	-64.9(0.1)[b]	42(0.5)	3.9(0.9)	0.8(0.4)	0.52(0.47)
			IRS 1 (Knez et al. 2008)		
C_2H_2	-55.9(0.2)	256(20)	0.8(0.1)	1.6(0.4)	6(0.7)
	-59.6(0.1)	205(11)	0.8(0.1)	1.8(0.3)	18(1.4)
HCN	-56.0(0.3)	202(22)	1.1(0.2)	17(8.5)	7.1(0.7)
	-59.9(0.1)	350(94)	0.6(0.2)	5.0(3.3)	9(2)
NH_3	-56.5(0.1)	194(25)	1.0(0.3)	16(11)	4.4(0.5)
	-59.8(0.2)	281(13)	0.8(0.3)	2.1(0.4)	14(5)
HNCO	-56.2(0.2)	377(47)	1.4(0.2)	0.29	2.4(0.3)
	-59.5(0.1)	190(10)	1.6(0.1)	0.24	8(1)

[a]Fixed equal to the temperature of C_2H_2 because an insufficient number of HCN lines were observed to constrain it.

[b]Fixed equal to v_{LSR} of C_2H_2 because HNCO was evidently not detected in the spectra but we sought upper limits on the other fitted parameters.

Table 4.3. 3σ upper limits to line equivalent width and column density of molecules in the upper state for selected non-detections. A uniform temperature of 200 K was assumed for all species.

Species/Mode	Line	n	W_{limit} (cm^{-1})	N_{limit}(X) (cm^{-2})
HNCO ν_4	1L-1L P branch	7	0.003	6.7×10^{19}
	1U-1U P branch	8	0.003	7.0×10^{19}
	0-0 P branch	6	0.003	8.4×10^{19}
	0-1L R branch	5	0.003	9.4×10^{19}
	0-0 R branch	5	0.003	6.8×10^{20}
$^{13}CH_4$ ν_4[a]	$R(1)$	1	0.003	4.1×10^{16}
	$R(4)$	4	0.003	3.1×10^{16}
OCS ν_2	P branch	34	0.003	2.9×10^{15}
HCN ν_2	R(15)	1	0.003	1.8×10^{16}
	$R(22)$	1	0.003	8.5×10^{16}
	$R(23)$	1	0.003	1.1×10^{17}
C_2H_2 ν_5	$R(12)$	1	0.003	8.5×10^{15}
	$R(21)$	1	0.003	9.4×10^{15}
	$R(22)$	1	0.003	3.5×10^{16}
C_2H_2 $2\nu_5$-ν_5	Q branch	15	0.004	2.1×10^{17}

[a]The given values of $N(^{13}CH_4)$ are for the isotopologue only rather than the total CH_4 column density.

was then computed according to

$$N(X) = \frac{W}{\alpha} \tag{4.9}$$

where α is the line strength for a particular transition. We used the GEISA line strengths where available and corrected them to a uniform temperature of 200 K as described previously. Results for our non-detections are given in Table 4.3.

We derived upper limits for all lines of a particular molecular species available in a given spectral setting, as indicated in the table by the number

of lines parameter n. In cases where $n > 1$, the equivalent width and column density upper limits given are simple averages. All limits are given with respect to the total number of molecules along the column irrespective of isotopic composition except for $^{13}CH_4$; here we have divided the derived column density by the terrestrial $^{12}C/^{13}C = 89$ ratio built into GEISA to recover the column density specifically for $^{13}CH_4$.

For HNCO, which is not included in GEISA, we calculated line strengths by multiplying the band strength, $A_{HNCO} = 7 \times 10^{-17}$ cm^{-1} molecule^{-1} cm^2, by the Hönl-London factors for each state. The band strength was obtained from van Broekhuizen et al. (2004b). A given column density of HNCO results in an equivalent width

$$W = \alpha N = A_{HNCO} \frac{J e^{-E_l/k_B T}}{k_B T/hcB} N, \tag{4.10}$$

where J is the lower state of the transition, E_l is the lower state energy, k_B is Boltzmann's constant, T is the temperature, h and c are Planck's constant and the speed of light, respectively, and B is the rotational constant of HNCO (=0.3666 cm^{-1}). The resulting column densities we derived for HNCO are dependent on assumed temperature, but the fact that none of the HNCO lines were clear detections leaves the temperature unconstrained. Our χ^2 fitting program (Section 4.1.2) preferred a comparatively low temperature of of 42 K for HNCO; this value lowers our column density upper limits by a factor of four compared to those computed for the 200 K adopted for all other species. Furthermore, the strengths of lines associated with the various types of transitions

of HNCO (detailed in Appendix A of Knez et al. 2008) depend either more or less strongly on temperature. Therefore, our HNCO limits are presented with the caveat that they are much less robust than if HNCO had been a clear detection. Given that weak lines of HNCO were seen in the spectrum of IRS 1, we included this molecule in our χ^2 minimization fitting of the IRS 9 data, fixing the LSR velocity equal to the fitted velocity of C_2H_2. By doing so we biased the program to find very weak lines of HNCO at expected positions, assuming any gas would be at the same velocity as acetylene, which was true for IRS 1. The values for some parameters preferred by `fitspec` are consistent with other observed molecules, such as the Doppler b parameter, (3.9±0.9) km s^{-1}. The excitation temperature, (42±0.5) K, is low compared to other species while the column density, (8±4)×10^{15} cm^2, is elevated compared to the IRS 1 results. The covering factor was unconstrained. `fitspec` returned a 1σ uncertainty of 3.5×10^{15} cm^{-2} for the HNCO column density, which is probably a better estimate of the upper limit than that given in Table 4.3.

4.1.4 An Upper Limit to the Ionizing Flux in IRS 9

Another non-detection in the TEXES data gives a useful upper limit. The $^2P_{1/2} \rightarrow {}^2P_{3/2}$ fine structure line of [Ne II] at approximately 780 cm^{-1} is a typical diagnostic of ionized gas at our wavelengths. The non-detection of this line in the spectrum of IRS 9 places a constraint on the amount of ionizing flux being emitted by the embedded central source.

Our analysis follows Ho & Keto (2007) who applied it to observations

of the mid-infrared [Ne II] and [Ne III] lines in external galaxies. The intensity of a spectral line is given generally as

$$I = \frac{h\nu_{21}A_{21}}{4\pi}\int n_2 dl, \tag{4.11}$$

in which A_{21} is the Einstein coefficient for spontaneous emission, $h\nu_{21}$ is the energy difference between the two levels, and n_2 is the number density of ions in the upper state. The relatively high critical density of [Ne II] (n_{crit} = 4.3×10^5 cm^{-3}; Petrosian 1970) means that the line flux is proportional to the emission measure; alternately, it depends on density in the same way as do recombination lines and free-free continuum radiation. Since the dominant de-exctiation method is radiative decay, the rate of emission, $A_{21}n_2$, can be approximated by the upward collisional rate alone. Ho and Keto give an approximate expression for the intensity of the [Ne II] line:

$$I_{[NeII]} = \frac{h\nu_{21}}{4\pi}\gamma f_+ C_{12} EM, \tag{4.12}$$

where γ is the abundance of Ne with respect to H in the interstellar medium, f_+ is the fraction of Ne in the singly ionized state and C_{12} is the upward collisional rate divided by the electron density n_e. With a similar expression for [Ne III], they derive an expression for the combined luminosity of both lines,

$$\begin{aligned} L_{[NeII]+[NeIII]} &= 3.16\times10^{42}(f_+ + 1.67f_{+2}) \\ &\times \left(\frac{D_L}{Mpc}\right)^2 \left(\frac{A}{sr}\right)\left(\frac{EM}{cm^{-6}pc}\right). \end{aligned} \tag{4.13}$$

In this equation, f_{+2} is the fraction of Ne in the doubly ionized state, D_L is the distance to the source, $A = \int d\Omega$ is the solid angle subtended by the source,

and EM $= \int {n_e}^2 dl$ is the emission measure. For the purposes of this calculation we assume none of the Ne is doubly ionized. The singly ionized fraction of Ne, 0.3, is taken from Figure 3 in Ho and Keto using for the radiation temperature the temperature of a ZAMS star with IRS 9's luminosity ($T_r = 26200$ K) and a ratio of the dilution factor for blackbody radiation, Γ, and n_e of 10^{-19} cm^3. Finally, the Ne line luminosity is related to the Lyman continuum luminosity by noting that, in equilibrium, the photoionization rate of hydrogen is equal to the recombination rate:

$$N_{ion} = n_e n_p \alpha_B V = A \alpha_B EM \tag{4.14}$$

where $\alpha_B = 2.6{\times}10^{-13}$ cm^3 s^{-1} is the recombination rate for "case B" recombination and V is the volume of the Ne emitting region. Equations 4.13 and 4.14 can be combined to relate the luminosity of the Ne lines to the photoionizing luminosity according to

$$L_{[NeII]+[NeIII]} = 4.15{\times}10^{-13}(f_+ + 1.67 f_{+2}){\times} f_{ion} N_{ion}, \tag{4.15}$$

in which f_{ion} is the fraction of ionizing photons absorbed by the gas, estimated by Hirashita et al. (2003) to be 0.6±0.2 in starburst galaxies. For am embedded source at higher dust density, f_{ion} is probably closer to 1, so we use this value.

At the position of the Doppler shifted [Ne II] line in our TEXES spectrum, the continuum flux density is 69.5±2.0 Jy, or $6.95{\times}10^{-22}$ erg s^{-1} cm^{-2} Hz^{-1}. To calculate the upper limit to the line luminosity we assumed a [Ne II] linewidth consistent with the widths of the molecular absorption features

observed toward IRS 9 but it is unclear whether this approach is reasonable; Lacy & Jaffe (2007) found that the [Ne II] line in IRS 1 had a width of ∼100 km s^{-1} they attribute to an ionized inner accretion disk. Such a broad line would be difficult to detect in IRS 9 with TEXES if it were weak, but the low flux of free-free emission and the lack of hydrogen recombination lines argue against any considerable amount of ionized material in the first place. Using the narrower linewidth estimate of 4 km s^{-1} and the 3.0 kpc distance to NGC 7538 given in Section 1.2, we find the 3σ line luminosity upper limit is 8×10^{21} erg s^{-1}. Neglecting the contribution of [Ne III] in Equation 4.15, we find a value of $N_{ion} = 1\times10^{35}$ photons s^{-1}. Tielens (2005) gives a value of the Lyman continuum photon luminosity $N_{Lyc} = 1.4\times10^{48}$ photons s^{-1} for a Main Sequence B0 star, well above the figure we calculated. Clearly photoionization does not provide any substantial amount of energy input to the radiation and thermal environments of IRS 9, unlike the apparent case of IRS 1.

4.2 Interpretation of the Spectroscopic Results

Interpretation of our results requires caution, given the underlying assumptions of the radiative transfer model in `fitspec` compared with the conditions presumed to exist in the envelopes of IRS 1 and IRS 9. The program assumes a single continuum source behind all absorbing material at a single, constant temperature along the line of sight. The column densities we report therefore do not represent the entire column to the embedded continuum source, but rather the column only to an effective "dust photosphere" interior

to which the optical depth is large at a given wavelength. Consequently, our observations at 5 μm probably probe to greater depth than those at 13 μm; while the optical depth may be lower at longer wavelengths, the colder, outer layers of the dusty region are likely too cool to emit significantly at 5 μm. Comparison of results at different wavelengths is therefore difficult. We can, however, draw some basic conclusions from the spectra.

We find that excitation temperatures for various molecules are basically consistent between the two sightlines with the exception of the hotter of the two HCN components toward IRS 1. That value of T_{ex} has a rather large uncertainty so it may in fact lie closer to $\sim$250 K. The column densities are also similar, though again with particular exception in the case of HCN. Knez et al. had the benefit of more HCN lines observed, but we find a column lower by at least a factor of five. Most striking is the disagreement between the two sources in terms of the intrinsic linewidths, but we do not mean to imply that thermal broadening in IRS 9 is the cause of its higher observed Doppler b values. At the least, we can say that the spectral lines observed in the direction of IRS 9 are generally less saturated than those seen toward IRS 1, and this has important consequences for the accuracy of the IRS 9 column densities we obtain.

An example in which saturation of lines becomes important is CO. Knez et al. (2008) derived fractional abundances relative to CO for a variety of molecules seen in absorption toward IRS 1, attempting to compensate for badly saturated ^{12}CO lines by using the value of $N(^{13}\mathrm{CO})$ in Mitchell et al.

(1990) and adopting $^{12}C/^{13}C = 45$ on the basis of their TEXES observations of IRS 1. The value of $N(^{13}CO)$ for IRS 9 reported by Mitchell et al. was based on their measurement of ^{12}CO lines and an assumed terrestrial ratio $^{12}C/^{13}C = 89$. Boogert et al. (2004) confirm the saturation of the ^{12}CO lines observed toward IRS 9, deriving an optical depth $\tau_{12} = 13 \pm 4$ assuming $^{12}C/^{13}C = 80$ from Boogert et al. (2002). However, they argue that reliable values for $N(^{12}CO)$ can be obtained, noting the ^{13}CO lines remain optically thin as well as the presence of $C^{18}O$ lines in their spectra and quote a value $N(^{12}CO) = (3.2\pm1.0)\times10^{18}$ cm^{-2}. While we may argue with their choice of $^{12}C/^{13}C$, their value of the CO column density is probably more realistic for IRS 9 than that obtained from the lower-resolution observations of Mitchell et al. (1990). The fractional abundances for some of the molecules we observed with TEXES, relative to CO, are shown in Table 4.4.

Similarly, an estimate of the abundance of various molecules with respect to H_2 can be made given a measurement of the quantity of dust along the line of sight and a value for the gas-to-dust ratio in a typical protostellar envelope. Knez et al. adopted an H_2 column density toward IRS 1 of 7.5×10^{22} cm^{-2} from Willner (1976) to calculate fractional abundances of other molecules; in the absence of an equivalent measurement toward IRS 9, we have done the same and present the results in the Table 4.4. The pattern of relative abundances differs between the objects, according to both the molecular species and whether the abundance of a given species is referred to CO or to H_2. The latter fact indicates that either the ratio of CO to H_2 or the gas-to-dust ratio

Table 4.4. Abundances in IRS 9 and IRS 1 with respect to CO and H_2

	IRS 9 (this work)		IRS 1 (Knez et al. 2008)	
Molecule	N(X)/N(CO)	N(X)/N(H_2)	N(X)/N(CO)	N(X)/N(H_2)
C_2H_2	1.2(-2)	5.2(-7)	5.4(-3)	4.5(-7)
HCN	5.0(-2)	2.1(-6)	3.5(-2)	2.9(-6)
NH_3	3.3(-2)	1.4(-6)	2.9(-2)	2.4(-6)
CH_4	4.5(-2)	4.5(-6)	1.4(-1)	1.2(-5)
HNCO	<2.5(-3)	<1.1(-7)	8.0(-4)	7.0(-8)

Note. — All values are given in the notation $A(B) = A \times 10^B$. The column densities toward IRS 1 adopted for CO and H_2 were $N(^{12}CO) = 6.3{\times}10^{18}$ cm^{-2} and $N(H_2) = 7.5{\times}10^{22}$ cm^{-2}. For IRS 9 the ^{12}CO column density used was $N(^{12}CO) = 3.2{\times}10^{18}$ cm^{-2}.

varies between objects.

The assumptions made in calculating the values in Table 4.4 – that the CO column density is comparable along both lines of sight and that the dust distribution and gas-to-dust ratio are similar in both cases – may not be unreasonable given that both objects are located in the same molecular cloud. Given this caveat, it is worth noting that the fractional abundances of all molecules relative to both CO and H_2 are broadly consistent with each other. C_2H_2 is more abundant in IRS 9 than 1, although this is only a suggestion in light of the assumptions. The apparent enhancement of HCN and NH_3 in IRS 1, however, appears a more robust conclusion. Values for the fractional abundance of HNCO are low in both cases, with the values given for IRS 9 set by the errors in N(HNCO) from `fitspec`.

Some kinematic information about IRS 9 is available in the lineshapes. In combination with the varying effective depths to which sightlines probe at different wavelengths, lineshapes give a sense of the distribution of various molecules along the line of sight The P Cygni line profiles of our CO observations, for example, clearly indicate expansion due to an outflow known previously. CH_4 absorption toward IRS 9 was known previously as well, but the TEXES data reveal the structure of the lines in more detail than the Keck+NIRSPEC spectra of Boogert et al. (2004). They argue that the abundance pattern of methane varies along the line of sight by at least an order of magnitude, with a low abundance in the outer envelope and outflow region and higher abundance in the warm inner envelope.

In contrast to the circumstellar disk model of IRS 1 presented in Knez et al. (2008) based on TEXES observations, we cannot establish the presence of a disk in IRS 9. However, our fitting program preferred relatively small covering factors, similar to those in the best-fit synthetic spectra for IRS 1. Knez et al. interpret this as the signature of a near edge-on disk, acting as a source of continuum radiation that is only partially covered by the absorbing material. Given the high velocity outflow in IRS 9 reported by Mitchell & Hasegawa (1991), we might rather be observing an accreting system nearly face-on in which the outflow both sweeps out a region near the continuum source and entrains material into the flow that only partially covers the source. This picture would account for the methane observations of Boogert et al. (2004) in which cold, solid-phase methane is seen in the outer envelope, becomes de-

pleted in the outflow, and is seen in the gas phase in the inner envelope, all along a single sightline.

4.3 A Radiative Pumping Scheme for NH_3

The TEXES observations of NH_3 lines toward IRS 9 show a pattern of emission and absorption, with dominant emission and weak, blueshifted absorption in the ν_2 P-branch lines and possible weak absorption ν_2 antisymmetric Q-branch. The latter fact may be explained by approximately equal amounts of absorption and emission in components of identical velocity nearly canceling each other. Significantly, however, these facts cannot be readily explained by simple radiative transfer involving pure absorption of radiation.

We propose to explain the observed a$P(4,K)$ line fluxes with a radiative transfer effect that involves preferential pumping of R-branch lines resulting in net emission on the P branch. The model assumes that the ammonia molecules are either exterior to a region of dust reprocessing the light of the embedded continuum source or mixed with the dust such that they are exposed to the spectrum of silicate dust emission. The molecules are shielded from direct exposure to any ionizing flux from the protostellar object by optically thick dust absorption at a visual extinction of dozens to hundreds of magnitudes, using the estimate of A_V of 60-90 for IRS 1 given in Knez et al. (2008). Lines in the ν_2 P, Q and R branches fall on different positions along the 9.7 μm silicate feature resulting in differing amounts of available flux to cause upward transitions on the three branches. As a result, more upward transitions occur

on the R branch, for example, than on P branch, but downward transitions have a roughly equal probability on all three branches. Thus the model predicts net absorption among the R-branch lines, net emission on the P branch, and no (or very weak) lines on the Q branch. This scheme assumes that all NH_3 transitions are due to radiative excitation and de-excitation only and that collisions between molecules or between molecules and dust grains are ignored. The model is time-independent and assumes the gas remains optically thin at all times.

We modeled gas is in a shell of thickness t around the continuum source with a NH_3 density n_{NH_3}. The rotational levels (J,K, s/a) were assumed to be populated thermally at temperature T. Electric dipole transitions to and from an upper vibrational level (J_u,K_u, s/a) proceed according to the selection rule that $\Delta K = 0$. In ammonia there is an additional requirement that the symmetry of the wavefunction change in the transition. This gives the permitted transitions a/s $R(J_u\text{-}1,K)$, a/s $Q(J_u,K)$ and a/s $P(J_u + 1,K)$. We obtained absorption coefficients α for each of these transitions from GEISA.

The absorption optical depth corresponding to the coefficient α is

$$\tau(\nu) = \alpha n_{NH_3} t \phi_\nu \tag{4.16}$$

in which ϕ_ν is the lineshape function, taken to be a simple Gaussian. Molecules are excited to the upper state along all branches at a rate

$$r_{up} = 4\pi {r_{in}}^2 \sum_{P,Q,R} \int \frac{F_o(\nu)}{h\nu} \tau(\nu) d\nu \tag{4.17}$$

per second, assuming $\tau \ll 1$ through the shell of thickness t. Here $F_o(\nu)$ is the incident continuum flux, which varies with ν, r_{in} is the inner radius of the shell, and h is Planck's constant. The rate at which photons are emitted on a given branch is determined by the rate of upward transitions and the branching ratio of the Einstein A coefficients, e.g.

$$r_{down} = r_{up} \frac{A_P}{A_P + A_Q + A_R} \tag{4.18}$$

for the P branch. We calculated values for the the A coefficients according to

$$A_{ul} = \frac{8\pi c}{\lambda^2} \alpha(T) \frac{Q_r}{g_u} e^{E_l/kT} \tag{4.19}$$

where λ is the wavelength of the transition, c is the speed of light, Q_r is the rotational partition function, g_u is the statistical weight of the upper state, E_l is the energy of the lower state, and k is Boltzmann's constant.

We used the branching ratios to compute the expected flux in a given line with wavenumber center w from

$$\sum_{P,Q,R} \frac{L_w}{hcw} N \alpha(T) \tag{4.20}$$

where L_w is the continuum luminosity near the line and N is the column density of ammonia molecules. This is the number of photons per second at line wavenumber w absorbed in the shell, which is then equal to the number of molecules making upward transitions in that line. Multiplying this by the branching ratio for a given branch then gives the number of downward transitions, equal to the number of emitted photons on that branch.

To judge whether this radiative transfer scheme is sufficient to explain the observations, we calculated the expected strengths of the NH_3 lines toward IRS 9. To begin, we required the relative intensity of the 10 μm dust emission feature at the frequency of each of the branches. We used the mid-infrared spectra of the young stars DI Cep and DK Tau obtained by Hanner et al. (1998) to which they fit models of optically thin silicate dust emission around the 9.7 μm feature. From these spectra we obtained relative intensities of 0.52, 0.78 and 1.00 for the P, Q and R branches, respectively. The intensities were normalized to the value on the R-branch as it is nearest the peak of the 10 μm feature. The observed continuum flux near the the P-branch lines, $\sim$60 Jy, was turned into a luminosity at the source by multiplying by $4\pi d^2$, where d is the distance to NGC 7538 (3.0 kpc). In doing so we have neglected the effect of interstellar extinction; the estimated $B-V$ color excess in the direction of IRS 9 is $E(B-V)$=28.7 from the maps of Schlegel et al. (1998). Assuming standard relations between $E(B\text{-}V)$ and A_V, this value implies A_V $\sim$ 100 magnitudes toward IRS 9; in turn, this gives $A_{12\mu m} \sim 2$ magnitudes.

The luminosity, $\sim 3\times10^{31}$ erg s^{-1} Hz^{-1} at the position of the R-branch lines, was scaled to the other branches according the values above. A column density of 1×10^{15} cm^{-2} was assumed, consistent with that derived from simple fits to the spectra in Chapter 4, along with a temperature of 100 K. Fluxes were calculated for lines originating from transitions beginning in the J=4 upper state of each branch; predictions are unavailable for lines that do not exist such as aQ(3,0). The predicted fluxes are the sum of the strengths of

Table 4.5 Predicted fluxes for the P, Q, R lines of ν_2 transitions of NH_3 ($J_u = 3$) and measured fluxes for the corresponding P-branch lines from TEXES spectra. Positive flux values indicate net emission while negative values indicate net absorption in a given line.

	Predicted			Observed
K	F_P (Jy)	F_Q (Jy)	F_R (Jy)	F_P (Jy)
0	0.031	–	-0.039	0.026
1	0.015	0.000	-0.020	0.013
2	0.010	-0.001	-0.018	–
3	0.008	-0.040	–	0.006

the predicted emission and absorption components of each line and show an overall pattern of emission on the P-branch, weak absorption to no lines on the Q-branch and absorption on the R-branch.

The line fluxes we computed are given in Table 4.5. The P-branch fluxes compare favorably with the integrated line fluxes from our data implying that our explanation is at least plausible. This suggests that the dust and NH_3 are in close proximity to one another.

Chapter 5

Summary

While a wealth of information is available about the physical and chemical evolution of low mass protostellar objects, the same information for their high-mass counterparts is lacking. Given the rate at which high-mass stars form, there are at any one time few candidate objects available for study, scattered widely across the galaxy and arising under a range of initial conditions. By studying coeval high mass protostellar objects in individual molecular clouds, we can control for initial physical and chemical conditions as the star formation process began and begin to understand what influences act on the environments of these stars as they form.

Here we have presented the method and results of a study of the embedded high mass protostellar objects NGC 7538 IRS 1 and IRS 9 with particular emphasis on the physical conditions within the envelope of IRS 9. We obtained high resolution, mid-infrared spectra of these objects in 46 ro-vibrational transitions of the fundamental bands of the molecules C_2H_2, CH_4, HCN, NH_3 and CO and a number of their isotopologues. We also detected two lines of the $\nu_4+\nu_5$ combination band of C_2H_2. From the spectra we derived excitation parameters and column densities for the various molecular species and com-

pared values for the two objects. We found broadly similar temperatures and fractional abundances for most species but find disparities that probably indicate differences in the radiation and/or thermal environment of both objects' envelopes as well as likely compositional differences. Despite establishing a low upper limit for the ionizing flux near IRS 9, our spectra of IRS 9 show comparable molecular abundances and temperatures. This leaves in doubt the heating source to account for those facts and invites further study to reveal the driving mechanism for IRS 9's chemistry.

Finally, our spectra of the P and Q branches of the ν_2 mode of NH_3 reveal a curious pattern of P-branch lines seen predominantly in emission and non-detection of the Q-branch lines. We interpret this as the result of a radiative transfer effect involving a mixture of NH_3 molecules and warm, emitting silicate dust grains which preferentially "pump" excitation of the molecules in the R branch. The branching ratios for downward transitions on the P, Q and R branches result in net absorption on the R-branch, net emission on the P branch, and nearly equal amounts of absorption and emission canceling on the Q-branch. Simple calculations using our NH_3 data show this scheme can quantitatively reproduce the effect we see. However, this result necessarily complicates our interpretation of molecular spectra in certain astrophysical situations and is worthy of additional research.

The data presented here are based in part on observations obtained at the Gemini Observatory, which is operated by the Association of Universities for Research in Astronomy, Inc., under a cooperative agreement with

the NSF on behalf of the Gemini partnership: the National Science Foundation (United States), the Science and Technology Facilities Council (United Kingdom), the National Research Council (Canada), CONICYT (Chile), the Australian Research Council (Australia), CNPq (Brazil) and SECYT (Argentina). Additional data were obtained at the Infrared Telescope Facility, which is operated by the University of Hawaii under Cooperative Agreement no. NNX08AE38A with the National Aeronautics and Space Administration, Science Mission Directorate, Planetary Astronomy Program.

This work was supported by National Science Foundation (NSF) grant AST-0607312.

Bibliography

Araya, E., Hofner, P., Goss, W. M., Linz, H., Kurtz, S., & Olmi, L. 2007, ApJS, 170, 152

Arnett, D. 1996, Supernovae and Nucleosynthesis: An Investigation of the History of Matter from the Big Bang to the Present (Supernovae and Nucleosynthesis: An Investigation of the History of Matter, from the Big Bang to the Present, by D. Arnett. Princeton: Princeton University Press, 1996.)

Balog, Z., Kenyon, S. J., Lada, E. A., Barsony, M., Vinkó, J., & Gáspaŕ, A. 2004, AJ, 128, 2942

Beichman, C. A., Neugebauer, G., Habing, H. J., Clegg, P. E., & Chester, T. J., eds. 1988, Infrared astronomical satellite (IRAS) catalogs and atlases. Volume 1: Explanatory supplement, Vol. 1

Bevington, P. R. & Robinson, D. K. 2003, Data reduction and error analysis for the physical sciences (Data reduction and error analysis for the physical sciences, 3rd ed., by Philip R. Bevington, and Keith D. Robinson. Boston, MA: McGraw-Hill, ISBN 0-07-247227-8, 2003.)

Boogert, A. C. A., Blake, G. A., & Öberg, K. 2004, ApJ, 615, 344

Boonman, A. M. S., van Dishoeck, E. F., Lahuis, F., & Doty, S. D. 2003, A&A, 399, 1063

Brunt, C. M. 2003, ApJ, 584, 293

Bryan, R. K. & Skilling, J. 1980, MNRAS, 191, 69

Campbell, B. 1984, ApJL, 282, L27

Charnley, S. B. 1995, Ap&SS, 224, 251

Collings, M. P., Anderson, M. A., Chen, R., Dever, J. W., Viti, S., Williams, D. A., & McCoustra, M. R. S. 2004, MNRAS, 354, 1133

Dartois, E., Demyk, K., d'Hendecourt, L., & Ehrenfreund, P. 1999, A&A, 351, 1066

De Buizer, J. M. & Minier, V. 2005, ApJL, 628, L151

Doty, S. D., Schöier, F. L., & van Dishoeck, E. F. 2004, A&A, 418, 1021

Draine, B. T. 2003, ARA&A, 41, 241

Evans, II, N. J., Lacy, J. H., & Carr, J. S. 1991, ApJ, 383, 674

Foster, T. & Routledge, D. 2003, ApJ, 598, 1005

Gibb, E. L., Whittet, D. C. B., Boogert, A. C. A., & Tielens, A. G. G. M. 2004, ApJS, 151, 35

Hanner, M. S., Brooke, T. Y., & Tokunaga, A. T. 1998, ApJ, 502, 871

Henkel, C., Wilson, T. L., & Johnston, K. J. 1984, ApJL, 282, L93

Heyer, M. H., Carpenter, J. M., & Snell, R. L. 2001, ApJ, 551, 852

Hirashita, H., Buat, V., & Inoue, A. K. 2003, A&A, 410, 83

Ho, L. C. & Keto, E. 2007, ApJ, 658, 314

Jacquinet-Husson, N., Scott, N. A., Chédin, A., Garceran, K., Armante, R., Chursin, A. A., Barbe, A., Birk, M., Brown, L. R., Camy-Peyret, C., Claveau, C., Clerbaux, C., Coheur, P. F., Dana, V., Daumont, L., Debacker-Barilly, M. R., Flaud, J. M., Goldman, A., Hamdouni, A., Hess, M., Jacquemart, D., Köpke, P., Mandin, J. Y., Massie, S., Mikhailenko, S., Nemtchinov, V., Nikitin, A., Newnham, D., Perrin, A., Perevalov, V. I., Régalia-Jarlot, L., Rublev, A., Schreier, F., Schult, I., Smith, K. M., Tashkun, S. A., Teffo, J. L., Toth, R. A., Tyuterev, V. G., Vander Auwera, J., Varanasi, P., & Wagner, G. 2005, Journal of Quantitative Spectroscopy and Radiative Transfer, 95, 429

Jiang, Z., Tamura, M., Hoare, M. G., Yao, Y., Ishii, M., Fang, M., & Yang, J. 2008, ApJL, 673, L175

Kameya, O. 2006, in Proceedings of the 8th European VLBI Network Symposium

Kameya, O., Morita, K.-I., Kawabe, R., & Ishiguro, M. 1990, ApJ, 355, 562

Knez, C., Lacy, J. H., Evans II, N. J., van Dishoeck, E. F., & Richter, M. J. 2008, submitted to ApJ

Kurtz, S., Cesaroni, R., Churchwell, E., Hofner, P., & Walmsley, C. M. 2000, Protostars and Planets IV, 299

Lacy, J. H., Faraji, H., Sandford, S. A., & Allamandola, L. J. 1998, ApJL, 501, L105+

Lacy, J. H. & Jaffe, D. T. 2007, in American Astronomical Society Meeting Abstracts, Vol. 211, American Astronomical Society Meeting Abstracts, #76.03+

Lacy, J. H., Richter, M. J., Greathouse, T. K., Jaffe, D. T., & Zhu, Q. 2002, PASP, 114, 153

Lahuis, F. & van Dishoeck, E. F. 2000, A&A, 355, 699

Lugo, J., Lizano, S., & Garay, G. 2004, ApJ, 614, 807

Michelson, A. A. 1898, ApJ, 8, 37

Mitchell, G. F. & Hasegawa, T. I. 1991, ApJL, 371, L33

Mitchell, G. F., Maillard, J.-P., Allen, M., Beer, R., & Belcourt, K. 1990, ApJ, 363, 554

Ojha, D. K., Tamura, M., Nakajima, Y., Fukagawa, M., Sugitani, K., Nagashima, C., Nagayama, T., Nagata, T., Sato, S., Vig, S., Ghosh, S. K., Pickles, A. J., Momose, M., & Ogura, K. 2004, ApJ, 616, 1042

Palumbo, M. E., Geballe, T. R., & Tielens, A. G. G. M. 1997, ApJ, 479, 839

Panagia, N. 1973, AJ, 78, 929

Pendleton, Y. J., Tielens, A. G. G. M., Tokunaga, A. T., & Bernstein, M. P. 1999, ApJ, 513, 294

Pestalozzi, M. R., Elitzur, M., Conway, J. E., & Booth, R. S. 2004, ApJL, 603, L113

Petrosian, V. 1970, ApJ, 159, 833

Reid, M. A. & Wilson, C. D. 2005, ApJ, 625, 891

Sandell, G., Goss, W. M., & Wright, M. 2005, ApJ, 621, 839

Scalo, J. & Elmegreen, B. G. 2004, ARA&A, 42, 275

Schlegel, D. J., Finkbeiner, D. P., & Davis, M. 1998, ApJ, 500, 525

Schöier, F. L., Jørgensen, J. K., van Dishoeck, E. F., & Blake, G. A. 2002, A&A, 390, 1001

Smith, R. L., Pontoppidan, K. M., Young, E. D., Morris, M. R., & van Dishoeck, E. F. 2007, in American Astronomical Society Meeting Abstracts, Vol. 211, American Astronomical Society Meeting Abstracts, #50.01+

Tielens, A. G. G. M. 2005, The Physics and Chemistry of the Interstellar Medium (The Physics and Chemistry of the Interstellar Medium, by A. G. G. M. Tielens, pp. . ISBN 0521826349. Cambridge, UK: Cambridge University Press, 2005.)

Ulich, B. L. & Haas, R. W. 1976, ApJS, 30, 247

van Broekhuizen, F. A., Keane, J. V., & Schutte, W. A. 2004a, A&A, 415, 425

—. 2004b, A&A, 415, 425

van der Tak, F. F. S., van Dishoeck, E. F., Evans, II, N. J., & Blake, G. A. 2000, ApJ, 537, 283

van Dishoeck, E. F. & Blake, G. A. 1998, ARA&A, 36, 317

Werner, M. W., Becklin, E. E., Gatley, I., Matthews, K., Neugebauer, G., & Wynn-Williams, C. G. 1979, MNRAS, 188, 463

Whittet, D. C. B., Schutte, W. A., Tielens, A. G. G. M., Boogert, A. C. A., de Graauw, T., Ehrenfreund, P., Gerakines, P. A., Helmich, F. P., Prusti, T., & van Dishoeck, E. F. 1996, A&A, 315, L357

Willner, S. P. 1976, ApJ, 206, 728

Zinnecker, H. & Yorke, H. W. 2007, ARA&A, 45, 481

Vita

John Caleb Barentine was born in Bagdad, Arizona on 22 November 1976, the son of John Bruce Barentine and Delsia Anne (Danley) Barentine. His career in astronomy began as an amateur when his interest was kindled by a family outing to Kitt Peak National Observatory in the summer of 1982. As a high school student his observing and outreach work won him runner-up recognition in the Astronomical League's National Outstanding Young Astronomer inaugural competition of 1993. He received a Bachelor of Science degree in Physics from the University of Arizona in 1998; while taking the degree he was employed as a research assistant at the National Optical Astronomy Observatories and National Solar Observatory in Tucson. He received a Master of Science degree in Physics from Colorado State University in 2002, writing a thesis on the use of small telescopes to carry out high precision photometric transit searches for extrasolar planets. In 2001 he joined the scientific staff at Apache Point Observatory in Sunspot, New Mexico as an Observing Specialist with the Astrophysical Research Consortium 3.5 m telescope. He went on to become an Observer for the Sloan Digital Sky Survey for two years beginning in 2004. He returned to graduate studies at the University of Texas in August 2006. The asteroid (14505) Barentine is named in his honor.

Permanent address: 407 A Swanee Dr
Austin, Texas 78752

This thesis was typeset with LaTeX[†] by the author.

[†]LaTeX is a document preparation system developed by Leslie Lamport as a special version of Donald Knuth's TeX Program.